Theory and Applications of Computational Chemistry: The First Forty Years
Edited by C. Dykstra et al.

CHAPTER 20

Recent advances in ab initio, *density functional theory, and relativistic electronic structure theory*

Haruyuki Nakano[1,2], Takahito Nakajima[1,3], Takao Tsuneda[1,4] and Kimihiko Hirao[1]

[1] *Department of Applied Chemistry, School of Engineering, University of Tokyo, Tokyo 113-8656, Japan*
[2] *Department of Chemistry, Graduate School of Sciences, Kyushu University, Fukuoka 812-8581, Japan*
[3] *PRESTO, Japan Science and Technology Agency (JST), 4-1-8 Honcho Kawaguchi, Saitama 332-0012, Japan*
[4] *Department of Quantum Engineering and Systems Science, School of Engineering, University of Tokyo, Tokyo 113-8656, Japan*

Abstract

Recent advances in electronic structure theory achieved in our group have been reviewed. Emphasis is put on development of *ab initio* multireference-based perturbation theory, exchange and correlation functionals in density functional theory, and molecular theory including relativistic effects.

20.1 INTRODUCTION

Accurate theoretical/computational chemistry has evolved dramatically and has opened up a world of new possibilities. It can treat real systems with predictive accuracy. Computational chemistry is becoming an integral part of chemistry research. Our research group, the University of Tokyo (UT) group, was founded in 1993. Since then the UT group has continued to grow and now becomes one of the centers of theoretical/computational chemistry. We are interested in theory development and application calculations. We have continued our research in the following three directions: (i) development of new *ab initio* theory, particularly multireference-based

References pp. 554–557

perturbation theory; (ii) development of exchange and correlation functionals in density functional theory (DFT); and (iii) development of molecular theory including relativistic effects. We have enjoyed good progress in each of the above areas. We are very excited about our discoveries of new theory and algorithms, and new findings in chemistry. We would like to share this enthusiasm with readers. The present review is a summary of our research activities which have been achieved in the last 10 years at the University of Tokyo.

20.2 MULTIREFERENCE PERTURBATION THEORY AND VALENCE BOND DESCRIPTION OF ELECTRONIC STRUCTURES OF MOLECULES

The development of multireference methods represents important progress in electronic structure theory in the last decades. The multiconfiguration self-consistent field (MCSCF) method, and configuration interaction (CI), coupled cluster (CC), and perturbation methods based on the MCSCF functions play a central role in the studies of electronic structure of molecules and chemical reaction mechanisms, especially in those concerned with electronic excited states.

Among several types of the MCSCF method, the complete active space self-consistent field (CASSCF) method is commonly used at present. In fact, it has many attractive features: (1) applicable to excited state as well as the ground state in a single framework; (2) size-consistent; (3) well defined on the whole potential energy surface if an appropriate active space is selected. However, CASSCF takes into account only non-dynamic electron correlation and not dynamic correlation. The accuracy in the energy such as excitation energy and dissociation energy does not reach the chemical accuracy, that is, within several kcal/mol. A method is necessary which takes into account both the non-dynamic and dynamic correlations for quantitative description.

Our multireference Møller–Plesset (MRMP) perturbation method [1–4] and MC-QDPT quasi-degenerate perturbation theory (QDPT) with multiconfiguration self-consistent field reference functions (MC-QDPT) [5,6] are perturbation methods of such a type. Using these perturbation methods, we have clarified electronic structures of various systems and demonstrated that they are powerful tools for investigating excitation spectra and potential energy surfaces of chemical reactions [7–10]. In the present section, we review these multireference perturbation methods as well as a method for interpreting the electronic structure in terms of valence-bond resonance structure based on the CASSCF wavefunction.

20.2.1 Multireference perturbation theory

Many-body perturbation theory (MBPT) has been utilized as a convenient way of taking account of electron correlation beyond the Hartree–Fock (HF) approximation. In particular, its single-reference version is now fully established. Møller–Plesset perturbation method [11], up to the fourth order, is provided as a standard tool in most

program systems such as GAUSSIAN or GAMESS. However, the application of the single-reference many-body perturbation theories (SR-MBPT) is limited only to the system where the Hartree–Fock approximation is a good starting point. It cannot describe open-shell molecules, dissociation to open-shell fragment, and transition state of chemical reaction.

Conventional QDPT [12–21] has been developed to be applied to open-shell systems and excited states. Although much effort has been made to develop the QDPT, it is not widely used among chemists. The major reason is that the QDPT often provides incorrect potential curves, since the perturbation series frequently diverges owing to the existence of intruder states [22].

In the 1980s and 1990s, multiconfigurational self-consistent field (MCSCF) reference perturbation theories [1–6,23–30] were proposed to overcome the defects of the single-reference PT and the QDPT, and now they are established as reliable methods that can be applied to wide variety of problems: potential energies surfaces of chemical reactions, excited spectra of molecules, etc. In fact, they have many advantages:

1. Generally applicable to a wide class of problems and a wide variety of molecules in a single framework;
2. Almost size-consistent;
3. Applicable to excited states and open-shells as well as the ground state;
4. Stable on the whole potential surface if reference CASSCF function is appropriately chosen;
5. Accurate enough to provide the chemical accuracy. Although MRMP and MC-QDPT at the lowest non-trivial order (the second order) does not yield very close total energy to the exact one, they are well balanced and the relative energies like dissociation energies, excitation energies, the activation energy are quite good.
6. Much more efficient and handy than MRCI and MRCC methods. The energy is computed as a sum of the product of molecular integrals and coupling constants between the target state and CSF divided by energy difference. The resource required does not depend strongly on the size of the active space and basis set. This presents a keen contrast to the case of MRCI and MRCC.

The MRMP method [1–4] and MC-QDPT [5,6] are perturbation methods in this category. In these methods, the CASSCF wavefunction(s) is(are) first determined, and the perturbation calculation is done with those wavefunctions used as reference (zeroth-order wavefunction) based on Rayleigh–Schrödinger PT in MRMP and van Vleck PT in MC-QDPT.

In the following sections, we show the formalism of the multireference perturbation theory and some applications to potential energy surfaces and electronic excited spectra.

20.2.1.1 Multireference Møller–Plesset perturbation method [1–4]

Our basic problem is to find approximations to some low-lying solutions of the exact Schrödinger equation

$$H\Psi = E\Psi \tag{1}$$

H is the Hamiltonian and it is decomposed into two parts, a zeroth-order Hamiltonian H_0 and a perturbation V

$$H = H_0 + V \tag{2}$$

We assume that a complete set of orthonormal eigenfunctions $\{\Psi_i^{(0)}\}$ and corresponding eigenvalues are available

$$H_0 \Psi_i^{(0)} = E_i^{(0)} \Psi_i^{(0)} \tag{3}$$

Then the state wavefunction Ψ_I is expanded in terms of basis functions $\Psi_k^{(0)}$ as

$$\Psi_I = \sum_k C_{Ik} \Psi_k^{(0)} \tag{4}$$

Some of the basis functions define an active space P and the remaining part of Hilbert space is called the orthogonal space $Q = 1 - P$. The active space is spanned by the basis functions that have a filled core and the remaining active electrons distributed over a set of active orbitals. The orthogonal complete space incorporates all other possible basis functions that are characterized by having at least one vacancy in a core orbital. The state wavefunction in an active space is written as

$$\Psi_I^{(0)} = \sum_k C_k \Phi_k \tag{5}$$

where the sum runs over active space basis functions $\{\Phi_i\}$ and C_k are the coefficients of only active space basis functions. It is convenient to use intermediate normalization, i.e.

$$\langle \Psi_I^{(0)} | \Psi_I^{(0)} \rangle = \langle \Psi_I^{(0)} | \Psi_I \rangle = 1 \tag{6}$$

We also assume that $\Psi_I^{(0)}$ is diagonal in P space

$$\langle \Psi_I^{(0)} | H | \Psi_J^{(0)} \rangle = \delta_{IJ} (E_I^{(0)} + E_I^{(1)}) \tag{7}$$

with

$$E_I^{(0)} = \langle \Psi_I^{(0)} | H_0 | \Psi_I^{(0)} \rangle \tag{8}$$

$$E_I^{(1)} = \langle \Psi_I^{(0)} | V | \Psi_I^{(0)} \rangle \tag{9}$$

The state-specific Rayleigh–Schrödinger perturbation theory based on the unperturbed eigenvalue equation

$$H_0 \Psi_I^{(0)} = E_I^{(0)} \Psi_I^{(0)} \tag{10}$$

leads to the first $E_I^{(k)}$ as

$$E_I^{(2)} = \langle \Psi_I^{(0)} | VRV | \Psi_I^{(0)} \rangle \tag{11}$$

$$E_I^{(3)} = \langle \Psi_I^{(0)} | VR(V - E_I^{(1)}) RV | \Psi_I^{(0)} \rangle \tag{12}$$

$$E_I^{(4)} = \langle \Psi_I^{(0)} | VR(V - E_I^{(1)})R(V - E_I^{(1)})RV | \Psi_I^{(0)} \rangle - E_I^{(2)}[\langle \Psi_I^{(0)} | VR^2V | \Psi_I^{(0)} |$$

$$+ \langle \Psi_I^{(0)} | VRH_0SH_0RV | \Psi_I^{(0)} \rangle], \text{ etc.} \tag{13}$$

The R and S are the resolvent operators

$$R = Q/(E_I^{(0)} - H_0) \tag{14}$$

$$S = P'/(E_I^{(0)} - H_0) \tag{15}$$

where $P' = P - |\Psi_I^{(0)}\rangle\langle\Psi_I^{(0)}|$.

The zeroth-order energies $E_I^{(0)}$ are given in terms of orbital energies as

$$E_I^{(0)} = \sum_{p\sigma} n_{p\sigma}(I)\varepsilon_{p\sigma} \tag{16}$$

where $\varepsilon_{p\sigma}$ and $n_{p\sigma}(I)$ are the energy of orbital p with spin σ and the occupation number of orbital p with spin σ in wavefunction Φ_I, respectively.

We have mainly used canonical Fock orbitals, which are defined so that the generalized Fock matrix

$$F_{pq} = h_{pq} + \sum_{rs} (D_{rs}^{\alpha} + D_{rs}^{\beta})[(pq|rs) - \tfrac{1}{2}(ps|rq)] \tag{17}$$

is partially diagonal in the core, active, and virtual orbital sub-blocks (D_{rs}^{α} and D_{rs}^{β} represent alpha and beta one-particle density matrices, respectively) and have adopted the diagonal elements of the generalized Fock matrix, F_{pp}, as orbital energies

$$\varepsilon_{p\alpha} = \varepsilon_{p\beta} = h_{pp} + \sum_{rs} (D_{rs}^{\alpha} + D_{rs}^{\beta})[(pp|rs) - \tfrac{1}{2}(ps|rp)] \tag{18}$$

However, in an open-shell system involving unpaired alpha electrons, the electron environment depends on whether the electron is in an alpha or a beta orbital. Thus, we have also proposed that we retain canonical Fock orbitals but adopt spin-dependent orbital energies defined by

$$\varepsilon_{p\alpha} = h_{pp} + \sum_{rs} \{D_{rs}^{\alpha}[(pp|rs) - (ps|rp)] + D_{rs}^{\beta}(pp|rs)\} \tag{19}$$

and

$$\varepsilon_{p\beta} = h_{pp} + \sum_{rs} \{D_{rs}^{\beta}[(pp|rs) - (ps|rp)] + D_{rs}^{\alpha}(pp|rs)\} \tag{20}$$

for alpha- and beta-spin orbitals, respectively [31].

When CASSCF wavefunction is used as the reference, the zeroth plus first-order energy $E_I^{(0)} + E_I^{(1)}$ is equal to the CASSCF energy. The lowest non-trivial order is, therefore, the second order. Let the reference function $|\Psi_{\alpha}^{(0)}\rangle$ be a CASSCF wavefunction

$$|\alpha\rangle = \sum_{\mathrm{A}} C_{\mathrm{A}} |\mathrm{A}\rangle \tag{21}$$

The energy up to the second order in MRMP is given by

$$E_\alpha^{(0-2)} = E_\alpha^{\mathrm{CAS}} + \sum_I \frac{\langle\alpha|V|I\rangle\langle I|V|\alpha\rangle}{E_\alpha^{(0)} - E_I^{(0)}} \tag{22}$$

where $\{|I\rangle\}$ is the set of all singly and doubly excited configurations from the reference configurations in CAS. The first term of the RHS is the CAS-CI energy.

20.2.1.2 Multiconfigurational quasi-degenerate perturbation theory (MC-QDPT) [5,6] We have also proposed a multistate multireference perturbation theory, the QDPT with MCSCF reference functions (MC-QDPT). In this PT, state-averaged CASSCF is first performed to set reference functions, and then an effective Hamiltonian is constructed, which is finally diagonalized to obtain the energies of interest.

The van Vleck PT for the CASSCF reference wavefunctions gives the order-by-order expansion of the effective Hamiltonian

$$(H_{\mathrm{eff}}^{(0-1)})_{\alpha\beta} = E_\beta^{\mathrm{CAS}}\delta_{\alpha\beta} \tag{23}$$

$$(H_{\mathrm{eff}}^{(2)})_{\alpha\beta} = \tfrac{1}{2}\langle\alpha|VRV|\beta\rangle + (\alpha \leftrightarrow \beta) \tag{24}$$

$$(H_{\mathrm{eff}}^{(3)})_{\alpha\beta} = \tfrac{1}{2}\langle\alpha|VR(V - E_\beta^{(0)})RV|\beta\rangle + (\alpha \leftrightarrow \beta), \text{ etc.} \tag{25}$$

where R is the resolvent operator given by Eq. (14). Thus, the effective Hamiltonian to second order is given by

$$(H_{\mathrm{eff}}^{(0-2)})_{\alpha\beta} = E_\beta^{\mathrm{CAS}}\delta_{\alpha\beta} + \frac{1}{2}\sum_I \left\{ \frac{\langle\alpha|V|I\rangle\langle I|V|\beta\rangle}{E_\beta^{(0)} - E_I^{(0)}} + \frac{\langle\beta|V|I\rangle\langle I|V|\alpha\rangle}{E_\alpha^{(0)} - E_I^{(0)}} \right\} \tag{26}$$

Substituting the second-quantized operator into V, we obtain an explicit formula using molecular integrals and orbital energies instead of matrix elements

$$\begin{aligned}(H_{\mathrm{eff}}^{(0-2)})_{\alpha\beta} = {} & E_\alpha^{\mathrm{CAS}}\delta_{\alpha\beta} - \sum_{pq,\mathrm{B}} \langle\alpha|E_{pq}|\beta\rangle C_{\mathrm{B}}(\beta) \sum_e \frac{u_{pe}u_{eq}}{\varepsilon_e - \varepsilon_q + \Delta E_{\mathrm{B}\alpha}} \\ & - \sum_{pqrs,\mathrm{B}} \langle\alpha|E_{pq,rs}|\mathrm{B}\rangle C_{\mathrm{B}}(\beta) \Bigg[\sum_e \frac{u_{pe}g_{eqrs}}{\varepsilon_e - \varepsilon_q + \varepsilon_r - \varepsilon_s + \Delta E_{\mathrm{B}\alpha}} \\ & + \sum_e \frac{g_{pers}u_{eq}}{\varepsilon_e - \varepsilon_q + \Delta E_{\mathrm{B}\alpha}} + \frac{1}{2}\sum_{(a,b)} \frac{g_{parb}g_{aqbs}}{\varepsilon_a - \varepsilon_q + \varepsilon_b - \varepsilon_s + \Delta E_{\mathrm{B}\alpha}} \Bigg] \\ & - \sum_{pqrstu,\mathrm{B}} \langle\alpha|E_{pq,rs,tu}|\mathrm{B}\rangle C_{\mathrm{B}}(\beta) \sum_e \frac{g_{pers}g_{eqtu}}{\varepsilon_e - \varepsilon_q + \varepsilon_t - \varepsilon_u + \Delta E_{\mathrm{B}\alpha}} + (\alpha \leftrightarrow \beta)\end{aligned} \tag{27}$$

with

$$g_{pqrs} = (pq|rs) \tag{28}$$

$$u_{pq} = (h_{pq} - \delta_{pq}\varepsilon_p) - \sum_i^{\mathrm{doc}} (2g_{pqii} - g_{piiq}) \tag{29}$$

and

$$\Delta E_{B\alpha} = E_B^{(0)} - E_\alpha^{(0)} \tag{30}$$

the difference between the energies of the zeroth-order state and configuration. The orbital labels $\{i\}$, $\{a\}$, and $\{e\}$ are for doubly occupied, active, and external orbitals, respectively, and $\{a', b'\}$ run over both active and external orbitals, and the suffix of the generator $\{p, q, r, s, t, u\}$ run over only active orbitals. The terms including doubly occupied orbitals are omitted in this equation. See Ref. [5] for the full formula.

This theory includes MRMP PT (the case that the set of reference functions reduces to a single function). Note that MRMP energy can be also calculated with the formula Eq. (27) by setting the number of the states to one.

20.2.1.3 Application of multireference perturbation theory to singlet–triplet splitting of CH_2 and CF_2 [31]

Many applications of the MRMP and MC-QDPT methods to chemical reactions and excitation spectra have been collected in our review articles [7–10]. Here we present the singlet–triplet splitting of CH_2 and CF_2: examples where the use of the spin-dependent orbital energies is crucial.

Various methods have been applied to the adiabatic singlet–triplet (ST) splitting of methylene with the same geometry, active space, and basis set given in Ref. [32]. We first calculated it with the same condition for comparison. The active space is a full-valence type CAS[6e,6o], and the basis set used is the double zeta plus polarization (DZP) basis. The results are listed in Table 20.1. The ST splitting by the original MRMP (MRMP with spin-averaged orbital energies, hereafter MRMP(SA)) is 15.9 kcal/mol; the deviation from the full CI value of 12.0 kcal/mol is 3.9 kcal/mol. This is improved by MRMP with spin-dependent orbital energies, MRMP(SD); the splitting is 12.6 kcal/mol, the discrepancy being only 0.6 kcal/mol.

We next carried out calculations with a larger basis set and active space to compare the calculated and experimental results. The splitting with Dunning's correlation consistent polarized valence triple zeta (cc-pVTZ) basis set is 10.1 kcal/mol, which is in good agreement with the experimental value of 9.4 kcal/mol [33]. In the calculations with CAS[6e,6o], even the reference CASSCF gives good results: 12.8 (DZP) and 10.5 (cc-pVTZ) kcal/mol. The deviation from the full CI and experimental values are only 0.8 and 1.1 kcal/mol, respectively. However, it is known that the energy splitting at the CASSCF level gets worse if the active space is enlarged to CAS[6e,12o]. We next calculated the splitting using CAS[6e,12o] as a further check. The result of CASSCF is 4.3 kcal/mol, which is rather poor compared with the CAS[6e,6o] value. On the contrary, the value 9.9 kcal/mol of MRMP(SD) is in much better agreement with experiment.

The geometry of CF_2 used in the calculations was determined with CASSCF [6e,6o]/cc-pVTZ. The active space and basis set for MRMP are CAS[12e,9o] and cc-pVTZ, respectively. The ST splitting energy calculated with MRMP(SD) is 52.6 kcal/mol. This is a fairly good estimate of the experimental value, 56.6 kcal/mol. [34] On the other hand, the value from MRMP(SA), 46.7 kcal/mol, is too small compared with experiment.

Table 20.1 Energy splitting between the $^1A_1$ and $^3B_1$ states in CH_2 and CF_2

Method	Energy (hartree)		ΔE (kcal/mol)
	$^1A_1$	$^3B_1$	
CH_2			
[6e,6o]CASSCF/DZP	−38.94532	−38.96578	12.8
[6e,6o]MRMP(SA)/DZP	−39.01106	−39.03636	15.9
[6e,6o]MRMP(SD)/DZP	−39.01106	−39.03115	12.6
Full CI/DZP	−39.02718	−39.04626	12.0
[6e,6o]CASSCF/cc-pVTZ	−38.95422	−38.97099	10.5
[6e,6o]MRMP(SA)/cc-pVTZ	−39.04461	−39.06778	14.5
[6e,6o]MROPT2/cc-pVTZ	−39.04461	−39.06138	10.5
[6e,6o]MRMP(SD)/cc-pVTZ	−39.04461	−39.06064	10.1
[6e,12o]CASSCF/cc-pVTZ	−39.02090	−39.02778	4.3
[6e,12o]MRMP(SA)/cc-pVTZ	−39.06931	−39.08723	11.2
[6e,12o]MROPT2/cc-pVTZ	−39.06931	−39.08513	9.9
[6e,12o]MRMP(SD)/cc-pVTZ	−39.06931	−39.08504	9.9
Exptl[a]			9.4
CF_2			
[12e,9o]CASSCF/cc-pVTZ	−236.85497	−236.76085	59.1
[12e,9o]MRMP(SA)/cc-pVTZ	−237.38184	−237.30738	46.7
[12e,9o]MROPT2/cc-pVTZ	−237.38184	−237.30391	48.9
[12e,9o]MRMP(SD)/cc-pVTZ	−237.38184	−237.29807	52.6
Exptl[b]			56.6

[a]Ref. [33].
[b]Ref. [34].

MROPT2 by Kozlowski and Davidson [29] also reproduces the splitting, 10.5 (CAS[6e,6o]) and 9.9 kcal/mol (CAS[6e,12o]) for CH_2. These numbers are very close to those of MRMP(SD). For CF_2, however, it gives a slightly smaller splitting of 48.9 kcal/mol.

20.2.1.4 Extension of reference wavefunctions—quasi-degenerate perturbation theory with quasi-complete active space self-consistent field reference functions (QCAS-QDPT) [35]

In the study of chemical reaction mechanisms, CAS-SCF method is a very useful approach and hence frequently used. However, CAS-SCF often generates far too many configurations, and the size of the active space outgrows the capacity of present technology. Perturbation methods using a selected reference configuration space but retaining the advantages of the CAS-based PTs are necessary.

We have proposed an MC-SCF method with a quasi-complete active space (QCAS), i.e. a QCAS-SCF method. In the MC-SCF method, we partition orbitals into core, active, and virtual, then construct the CI space by distributing active electrons among the active orbitals. Let us further divide the active electron and orbital sets into N sub-sets and fix

the number of active electrons, m_i, and orbitals, n_i, in each sub-set

$$m_{\mathrm{act}} = \sum_{i}^{N} m_i, \qquad n_{\mathrm{act}} = \sum_{i}^{N} n_i \tag{31}$$

where m_{act} and n_{act} denote the number of active electrons and orbitals, respectively. We define the quasi-complete space as the product space of CAS spanned by the determinants or CSF as follows:

$$\mathrm{QCAS}(\{m_i\},\{n_i\}) = \mathrm{CAS}(m_1,n_1)\mathrm{CAS}(m_2,n_2)\cdots\mathrm{CAS}(m_N,n_N) \tag{32}$$

such that the number of electrons in each orbital group satisfies the restriction in Eq. (31).

Combining QCAS with MC-QDPT provides an effective tool for electronic structure theory. We present MC-QDPT using QCAS-SCF reference functions. (Hereafter, we call it QCAS-QDPT or QCAS-PT.)

Adopting (state-averaged) QCAS-SCF wave functions $\alpha(\beta)$ as reference functions (i), which define P space, we obtain the effective Hamiltonian to the second order

$$(H_{\mathrm{eff}}^{(0-2)})_{\alpha\beta} = E_{\alpha}^{\mathrm{QCAS}}\delta_{\alpha\beta} + \frac{1}{2}\left\{\sum_{I\notin\mathrm{QCAS}} \frac{\langle\alpha|V|I\rangle\langle I|V|\beta\rangle}{E_{\beta}^{(0)} - E_{I}^{(0)}} + (\alpha\leftrightarrow\beta)\right\} \tag{33}$$

which corresponds to Eq. (26) in the CAS-SCF reference case. Let us define a *corresponding complete active space* (CCAS) to a QCAS as the complete active space (CAS) that has the same active orbital set and electron but does not have the limitation (Eq. (31)). In other words, the corresponding CAS is the minimal CAS that includes the QCAS. Then the summation for I in Eq. (33) may be divided into the summations for determinants/CSFs outside the CAS and for the determinants/CSFs outside the QCAS but inside the corresponding CAS

$$\sum_{I\notin\mathrm{QCAS}} = \sum_{I\notin\mathrm{CCAS}} + \sum_{I\in\mathrm{CCAS}\wedge I\notin\mathrm{QCAS}} \tag{34}$$

and then the former second-order term in Eq. (33) may be written as

$$(H_{\mathrm{eff}}^{(2)})_{\alpha\beta} = \sum_{I\notin\mathrm{CCAS}} \frac{\langle\alpha|V|I\rangle\langle I|V|\beta\rangle}{E_{\beta}^{(0)} - E_{I}^{(0)}} + \sum_{I\in\mathrm{CCAS}\wedge I\notin\mathrm{QCAS}} \frac{\langle\alpha|V|I\rangle\langle I|V|\beta\rangle}{E_{\beta}^{(0)} - E_{I}^{(0)}} \tag{35}$$

The former term in Eq. (35) involves excitations from core orbitals and excitations to virtual orbitals in the intermediate states I (the *external* terms), while the latter term involves excitations where only active orbitals are involved (the *internal* terms).

The external term may be further written as

$$(H_{\mathrm{ext}}^{(2)})_{\alpha\beta} = \sum_{\mathrm{A,B}\in\mathrm{QCAS}} C_{\mathrm{A}}(\alpha)C_{\mathrm{B}}(\beta)(H_{\mathrm{ext}}^{(2)})_{\mathrm{AB}} \tag{36}$$

with

$$(H_{\mathrm{ext}}^{(2)})_{\mathrm{AB}} = \sum_{I \notin \mathrm{CCAS}} \frac{\langle \mathrm{A}|H|I\rangle\langle I|H|\mathrm{B}\rangle}{E_{\mathrm{B}}^{(0)} - E_I^{(0)} + (E_\beta^{(0)} - E_{\mathrm{B}}^{(0)})} \tag{37}$$

where $(H_{\mathrm{ext}}^{(2)})_{\mathrm{AB}}$ is the effective Hamiltonian in the determinant/CSFs basis in the conventional QDPT except for the energy shift, $E_\beta^{(0)} - E_{\mathrm{B}}^{(0)}$, in the denominator. Since the second-order diagrams do not depend on the denominator, the second-order effective Hamiltonian equation (37) (hence, also Eq. (36)) is expressed by the same diagrams as the conventional QDPT. This situation is the same as MC-QDPT: the diagrams and the rule for translating them into mathematical expressions is described in detail in Ref. [35]. The internal terms are also expressed by diagrams. Since QCAS is a natural extension of CAS, computation of these diagrams can be done efficiently in a similar manner to CAS-QDPT.

20.2.1.5 Further extension of reference wavefunctions—quasi-degenerate perturbation theory with general-multiconfiguration space self-consistent field reference functions (GMC-QDPT) [36]

Adopting (state-averaged) general MC-SCF (or MC-CI) wavefunctions $\alpha(\beta)$ as reference functions $\Phi_{\mathrm{A}}^{(0)}$ ($\Phi_{\mathrm{B}}^{(0)}$), which define the P space, the effective Hamiltonian to the second order becomes

$$(H_{\mathrm{eff}}^{(0-2)})_{\alpha\beta} = E_\alpha^{\mathrm{MC}}\delta_{\alpha\beta} + \frac{1}{2}\left\{\sum_{I \notin \mathrm{GCS}} \frac{\langle\alpha|H|I\rangle\langle I|H|\beta\rangle}{E_\beta^{(0)} - E_I^{(0)}} + (\alpha \leftrightarrow \beta)\right\} \tag{38}$$

where I is now a determinant/CSF outside the general configuration space (GCS). The notation $(\alpha \leftrightarrow \beta)$ means interchange α with β from the first term in curly brackets. The complementary eigenfunctions of the MC-CI Hamiltonian and the determinants/CSFs generated by exciting electrons out of the determinants/CSFs in GCS are orthogonal to the reference functions and define the Q space. The functions in the space complementary to the P space in GCS, however, do not appear in Eq. (38) since the interaction between the complementary functions and the reference functions is zero.

The GMC-QDPT computation scheme is similar to that of QCAS-QDPT [35]. We define again the corresponding CAS (CCAS) as a CAS constructed from the same active electrons and orbitals, that is, the minimal CAS that includes the reference GCS. The summation over I in Eq. (38) may be divided into the summations over determinants/CSFs outside CCAS and over the determinants/CSFs outside the GCS but inside CCAS:

$$\sum_{I \notin \mathrm{GCS}} = \sum_{I \notin \mathrm{CCAS}} + \sum_{I \in \mathrm{CCAS} \wedge I \notin \mathrm{GCS}} \tag{39}$$

then the former second-order term in Eq. (38) may be written as

$$(H_{\mathrm{eff}}^{(2)})_{\alpha\beta} = \sum_{I \notin \mathrm{CCAS}} \frac{\langle\alpha|H|I\rangle\langle I|H|\beta\rangle}{E_\beta^{(0)} - E_I^{(0)}} + \sum_{I \in \mathrm{CCAS} \wedge I \notin \mathrm{GCS}} \frac{\langle\alpha|H|I\rangle\langle I|H|\beta\rangle}{E_\beta^{(0)} - E_I^{(0)}} \tag{40}$$

The first term in Eq. (40) represents external excitations, while the latter term represents internal excitations.

The external terms may be computed with diagrams in the same manner as the QCAS-QDPT case. On the other hand, for internal terms, the diagrammatic approach may not be applied. Instead, matrix operations for the Hamiltonian matrix are used

$$(H^{(2)}_{\text{int}})_{\alpha\beta} = \mathbf{v}^{\text{T}}(\alpha) \cdot \mathbf{w}(\beta) \tag{41}$$

with

$$\mathbf{v}_I(\alpha) = \sum_{\text{A}\in\text{GCS}} \langle I|H|\text{A}\rangle C_{\text{A}}(\alpha) \tag{42}$$

$$\mathbf{w}_I(\beta) = \sum_{\text{B}\in\text{GCS}} \langle I|H|\text{B}\rangle C_{\text{B}}(\beta)/(E^{(0)}_{\beta} - E^{(0)}_{\text{B}}) \tag{43}$$

The intermediate determinants/CSFs I are constructed by exciting one or two electron(s) from the reference determinants/CSFs within the active orbital space. In general, the number of I is not large, and thus they may be managed in computer memory.

20.2.1.6 Application of QCAS- and GMC-QDPT

20.2.1.6.1 Transition state barrier height for the unimolecular dissociation reaction of formaldehyde $H_2CO \rightarrow H_2 + CO$ [35]. This reaction is Woodward–Hoffmann forbidden, and therefore, proceeds *via* the highly asymmetric transition structure. We examined in a previous paper [37] the barrier height using the MRMP method. In the present section, we show the QCAS-PT results and the comparison of them with the MRMP results.

The CAS we used for comparison is CAS(12,10), which is the full valence active space. We split the active orbitals into {CO(σ, σ^*)}, {CO(π, π^*)}, and {CH(σ, σ^*), CH(σ', σ'^*), O(lp, lp)}, where lp denotes a lone pair orbital, and then we distributed two, two, and eight electrons among the above groups, respectively, to construct QCAS[$(2,2)^2 \times (8,6)$]. The dimension of the CAS is 44,100, while that of the QCAS is 3600.

The results with cc-pVTZ and cc-pVQZ are shown in Table 20.2. First let us compare the results at the reference function (QCAS- and CAS-SCF) level. Although differences in the energy itself between QCAS-SCF and CAS-SCF are about 10 millihartree for both basis sets, the differences in the barrier height are 1.65 and 1.62 millihartree (1.0 and 1.0 kcal/mol) for cc-pVTZ and cc-pVQZ, respectively. The agreement of QCAS-SCF with CAS-SCF is very good.

Now let us compare the results at the multireference PT level. In total energy, there still remains a difference of about 8 millihartree between the results of QCAS-PT and MRMP. In relative energy, for the barrier height the QCAS-PT results are very close to those of CAS-PT in both basis sets. The barrier height of QCAS-PT is 83.7 kcal/mol in both basis sets, the differences from those of MRMP are only 0.1 and 0.3 kcal/mol for cc-pVTZ and cc-pVQZ, respectively. Moreover, the barrier height is also close to the experimental value, 84.6 kcal/mol [38]. The error of 0.9 kcal/mol is within twice the experimental uncertainty 0.8 kcal/mol.

Table 20.2 Transition state barrier height for the reaction $H_2CO \rightarrow H_2 + CO$

	Eq. (hartree)[a]	Tr. (hartree)[b]	ΔE (kcal/mol)	Error (kcal/mol)
cc-pVTZ				
CAS-SCF	−114.04696	−113.91381	83.6	−1.0
QCAS-SCF	−114.03786	−113.90306	84.6	0.0
MRMP	−114.30451	−114.17134	83.6	−1.0
QCAS-PT	−114.29674	−114.16338	83.7	−0.9
cc-pVQZ				
CAS-SCF	−114.05624	−113.92300	83.6	−1.0
QCAS-SCF	−114.04712	−113.91226	84.6	0.0
MRMP	−114.33057	−114.19763	83.4	−1.2
QCAS-PT	−114.32316	−114.18981	83.7	−0.9
Exptl. (classical)[c]			84.6 ± 0.8	

[a]Equilibrium structure.
[b]Transition state structure.
[c]Ref. [38]. Barrier height not including zero-point energy correction.

20.2.1.6.2 Valence excitation energies for formaldehyde [36]. The second example is the GMC-QDPT calculation of valence excitation energies for formaldehyde molecule. Calculations on formaldehyde were carried out at the ground state experimental geometry (i.e. $r(CO) = 1.203$ Å, $r(CH) = 1.099$ Å, and $\theta(HCH) = 116.5°$). The basis set used was Dunning's cc-pVTZ.

Five reference spaces were constructed from eight electrons, 16 $[(a_1, a_2, b_1, b_2) = (7,1,3,5)]$, 18 $[= (7,1,4,6)]$, 20 $[= (8,1,5,6)]$, 22 $[= (8,2,5,7)]$, and 24 orbitals $[= (9,2,6,7)]$, by exciting one and two electrons from the following parent configurations:

$^1A_1$ states : $\ldots n^2(\mathrm{HF})$; $\pi \rightarrow \pi^*$; $n \rightarrow \sigma^*$

$^3A_1$ states : $\pi \rightarrow \pi^*$; $n \rightarrow \sigma^*$

$^{1,3}A_2$ states : $n \rightarrow \pi^*$; $1b_2(\sigma) \rightarrow \pi^*$

$^{1,3}B_1$ states : $5a_1(\sigma) \rightarrow \pi^*$

$^{1,3}B_2$ states : $n \rightarrow 6a_1(\sigma^*)$

All the calculations were done in each symmetry.

The results are summarized in Tables 20.3 and 20.4. The calculations with CAS-SCF and CAS-QDPT are far too large to be done. We, therefore, compare the results with available experimental results and some recent theoretical results, i.e. MR-CI results by Hachey et al. [39], the second-order complete active space perturbation theory (CASPT2) calculations by Merchán and Roos [40], and the equation of motion coupled cluster (EOM-CC) calculations by Gwaltney and Bartlett [41].

As can be computed from Table 20.3, the maximum differences in excitation energy for the largest three (two) numbers of active orbitals is 0.09 (0.05) eV. We can, therefore, consider that the excitation energies at the MC-SCF level are almost converged values for

Table 20.3 Valence excitation energies of H_2CO (eV)

State	Orbital picture	MC-SCF					GMC-QDPT					Exptl
		(8,16)	(8,18)	(8,20)	(8,22)	(8,24)	(8,16)	(8,18)	(8,20)	(8,22)	(8,24)	
$^1A_1$	$\pi \rightarrow \pi^*; n \rightarrow \sigma^*$	10.07	10.03	10.03	10.02	10.02	9.66	9.67	9.72	9.72	9.72	
	$n \rightarrow \sigma^*; \pi \rightarrow \pi^*$	11.01	11.01	11.00	11.03	11.01	10.65	10.63	10.65	10.63	10.64	10.70
$^1A_2$	$n \rightarrow \pi^*$	4.32	4.43	4.27	4.25	4.22	4.04	4.02	4.01	4.02	4.08	4.07
	$1b_2(\sigma) \rightarrow \pi^*$	10.96	11.16	10.97	10.98	10.94	10.30	10.34	10.33	10.37	10.43	
$^1B_1$	$5a_1(\sigma) \rightarrow \pi^*$	9.63	9.89	9.82	9.81	9.80	9.31	9.24	9.26	9.20	9.28	9.00
$^1B_2$	$n \rightarrow 6a_1(\sigma^*)$	7.73	8.16	8.22	8.32	8.31	8.31	8.23	8.41	8.45	8.45	
$^3A_1$	$\pi \rightarrow \pi^*; n \rightarrow \sigma^*$	6.18	6.28	6.19	6.13	6.11	6.13	6.13	6.18	6.17	6.18	6.00
	$n \rightarrow \sigma^*; \pi \rightarrow \pi^*$	9.66	9.64	9.70	9.74	9.75	9.60	9.61	9.62	9.62	9.62	
$^3A_2$	$n \rightarrow \pi^*$	3.84	3.95	3.78	3.75	3.71	3.63	3.58	3.58	3.61	3.63	3.50
	$1b_2(\sigma) \rightarrow \pi^*$	10.52	10.68	10.52	10.52	10.47	10.04	10.03	10.02	10.07	10.10	
$^3B_1$	$5a_1(\sigma) \rightarrow \pi^*$	8.78	9.02	8.92	8.91	8.90	8.45	8.41	8.39	8.27	8.50	8.50
$^3B_2$	$n \rightarrow 6a_1(\sigma^*)$	7.36	7.79	7.85	7.95	7.94	7.89	7.80	7.99	8.02	8.07	

References pp. 554–557

Table 20.4 Valence excitation energies of H_2CO (eV)

State	Orbital picture	MC-SCF (8,24)	GMC-QDPT (8.24)	Exptl	MRCI[a]	CASPT2[b]	EOM-CC[c]	CCSD[d]	CIS-MP2[e]	SAC-CI[f]
$^1A_1$	$\pi \rightarrow \pi^*$, $n \rightarrow \sigma^*$	10.02	9.72		9.60	9.77	9.47	9.27	9.19	–
	$n \rightarrow \sigma^*$, $\pi \rightarrow \pi^*$	11.01	10.64	10.70						10.83
$^1A_2$	$n \rightarrow \pi^*$	4.22	4.08	4.07	4.05	3.91	3.98	3.95	4.58	4.16
	$1b_2(\sigma) \rightarrow \pi^*$	10.94	10.43				10.38		10.08	11.19
$^1B_1$	$5a_1(\sigma) \rightarrow \pi^*$	9.80	9.28	9.00	9.35	9.09	9.33	9.26	9.97	9.49
$^1B_2$	$n \rightarrow 6a_1(\sigma^*)$	8.31	8.45							
$^3A_1$	$\pi \rightarrow \pi^*$; $n \rightarrow \sigma^*$	6.11	6.18	6.00		5.99			6.72	6.10
	$n \rightarrow \sigma^*$;$\pi \rightarrow \pi^*$	9.75	9.62							
$^3A_2$	$n \rightarrow \pi^*$	3.71	3.63	3.50		3.48			4.15	3.70
	$1b_2(\sigma) \rightarrow \pi^*$	10.47	10.10						10.52	10.80
$^3B_1$	$5a_1(\sigma) \rightarrow \pi^*$	8.90	8.50	8.50					9.18	8.52
$^3B_2$	$n \rightarrow 6a_1(\sigma^*)$	7.94	8.07							

[a]Ref. [39].
[b]Ref. [40].
[c]Ref. [41].
[d]Ref. [42].
[e]Ref. [43].
[f]Ref. [44].

the change of the active orbital numbers. However, the agreement with the experimental values is not so good: the error is 0.32 eV on average and 0.80 eV at maximum.

At the GMC-QDPT level, the excitation energies are also almost converged (though the differences are a little larger than those at MC-SCF level are). Compared to the reference MC-SCF level, the results are somewhat improved. The error from the experimental value was reduced to 0.11 eV on average and 0.28 eV at maximum.

20.2.1.6.3 The most stable structure of SiC_3 [45]. Silicon-containing carbon clusters, Si_mC_n, have recently received much attention from various fields, such as astrophysics and nanoscience. In particular, SiC_n ($n = 1-4$) molecules have been well studied, both experimentally and theoretically. However, among the theoretical studies, the most stable structure of SiC_3 was in dispute. The most stable structure of the SiC_3 molecule was investigated using second-order perturbation theory with general multiconfiguration self-consistent field reference functions (GMC-PT).

The basis sets used were Dunning's cc-pVXZ (X = D, T, Q) and augmented cc-pVXZ (X = D, T, Q) basis sets. Using these basis sets, we first carried out Hartree–Fock (HF) calculations (unrestricted HF calculations for 1t and restricted HF calculations for 2s and 3s; see Fig. 20.1). The active spaces in the reference MC-SCF calculations were constructed from the HF configuration plus single and double excitation configurations among valence orbitals, that is, valence configuration interaction singles and doubles (CISD) space. The 16 electrons in the 16 orbitals were correlated in MC-SCF calculations; hereafter, we refer to these spaces as MC(16,16) following the CAS(n, m) notation.

Table 20.5 shows the relative stability of the 1t, 2s, and 3s isomers. The results indicate that the 2s isomer is most stable in all the basis sets and at both the CCSD(T) and

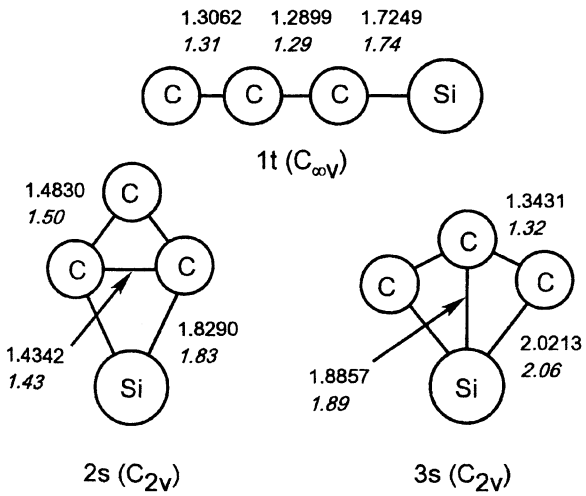

Fig. 20.1. Three isomers of SiC_3: 1t, 2s, and 3s. The numbers in roman and italic type represent the bond lengths in ångstrom optimized by CCSD(T)/cc-pCVQZ (Refs. [47,49]) and FORS-SCF/6-31G(d) (Ref. [46]) methods, respectively.

Table 20.5 Relative energy of the 1t and 3s isomers measured from the energy of the 2s isomer (in kcal/mol)

Structure	cc-pVXZ sets			aug-cc-pVXZ sets			CCSD(T)[a] (cc-pCVQZ)	MC-QDPT[b] (aug-cc-pVDZ)
	X = D	X = T	X = Q	X = D	X = T	X = Q		
CCSD(T) geometry								
1t (SD)	3.4	5.1	6.3	3.7	5.4	6.7 (7.2)[c]	7.5 (8.0)[c]	–
1t (SA)	−1.1	−0.4	0.7	−1.6	−0.4	0.9 (1.4)[c]		–
2s	0.0	0.0	0.0	0.0	0.0	0.0	0.0	–
3s	4.2	4.9	5.3	3.4	4.8	5.3 (5.1)[c]	6.2 (6.0)[c]	–
FORS-SCF geometry								
1t (SD)	4.6	7.3	8.8	5.5	7.9	9.9 (9.9)[d]	–	–
1t (SA)	0.1	1.8	3.0	0.3	2.1	3.9 (4.0)[d]	–	−4.4 (−4.3)[d]
2s	0.0	0.0	0.0	0.0	0.0	0.0	–	0.0
3s	7.3	8.5	9.0	6.6	7.7	9.0 (8.7)[d]	–	3.4 (3.1)[d]

[a]Refs. [47,49].

[b]Ref. [46].

[c]The numbers in the parentheses are zero point corrected energies. The zero point vibrational energies are taken from Ref. [47].

[d]The numbers in the parentheses are zero point corrected energies. The zero point vibrational energies are taken from Ref. [46].

CAS-SCF geometries except for some spin-averaged orbital energy numbers. The second most stable isomer is the 3s isomer, although the energy difference from the 1t isomer is quite small. The relative energy of the 3s isomer measured from the 2s isomer was 5.3 (9.0) kcal/mol in the calculations with the aug-cc-pVQZ basis and CCSD(T) (CAS-SCF) geometry, while the relative energy of the 1t isomer was 6.7 (9.9) kcal/mol. This order of the isomers is unchanged even though the zero-point vibrational energy (ZPVE) correction is included. The ZPVEs for the 1t, 2s, and 3s isomers are very close to one another: 7.41, 7.37, and 7.07 kcal/mol, respectively, at the CAS-SCF level [46]. (The differences of ZPVEs at the CCSD level are $E_{ZPV}(1t) - E_{ZPV}(2s) = 0.5$ kcal/mol and $E_{ZPV}(3s) - E_{ZPV}(2s) = -0.2$ kcal/mol at the CCSD level [47]. ZPVEs themselves were not reported in Ref. [47]). The zero-point corrected energies are also listed in Table 20.5.

Table 20.5 also tells us a clear trend of the basis set effect, with a larger basis set giving larger 2s−3s and 2s−1t energy separations. This implies that the most stable isomer will not change if we use larger basis sets than those used. To check the basis set effect on the order of the isomers, we calculated the complete basis set limits. The complete basis set extrapolation of the CCSD energy is given by the Gaussian dependence [48] on basis set sizes, i.e.

$$E(n) = E(\infty) + E_0 \exp[-(n-1)] + E_1 \exp[-(n-1)^2] \tag{44}$$

where n is the cardinal number of the basis set (2, 3, 4 for DZ, TZ, QZ, respectively), $E(\infty)$ is the complete basis set limit, and E_0 and E_1 are constants. By assuming the basis set dependence of GMC-PT is the same, apart from a multiplicative factor, we extrapolated the energy in the complete basis set. The relative energies at the complete

basis set limit, computed through the above extrapolation, were 7.6 (11.1) and 5.6 (9.9) kcal/mol for the 1t and 3s isomer, respectively, in the CCSD(T) (FORS-SCF) geometry. The relative order of the 1t and 3s isomers was unchanged which supports our conclusion that the 2s isomer is most stable.

20.2.2 Valence bond description of complete active space self-consistent field function

A defect of the multireference-based methods is that the wavefunction is too complicated to extract chemical description from it. There are too many CI coefficients, cluster amplitudes, or terms corresponding to diagrams in those methods. The information of the chemical picture is hidden behind them and to extract it seems quite difficult.

Classical valence bond (VB) theory is very successful in providing a qualitative explanation for many aspects. Chemists are familiar with the localized molecular orbitals (LMO) and the classical VB resonance concepts. If modern accurate wave functions can be represented in terms of such well-known concepts, chemists' intuition and experiences will give a firm theoretical basis and the role of the computational chemistry will undoubtedly expand.

The CASVB functions [50,51] can be obtained by transforming the canonical CASSCF functions without loss of energy. First we transform the CASSCF delocalized MO to localized MO using the arbitrariness in the definition of the active orbitals. Then we perform a full CI again in the active space. The CASVB method provides an alternative tool for describing the correlated wave functions.

Similar approaches have been employed by various workers. Lam et al. [52] showed that wave functions in FORS can be expressed in terms of localized configuration-generating MOs which have essentially atomic character. Cundari et al. [53] extended the idea and used it successfully to study the high-valent transition metal complexes. They used the orthogonal spin functions generated by the Kotani–Yamanouchi branching diagrams. Also our method has some relation to the spin-coupled valence bond (SCVB) method of Cooper et al. [54,55], where the spin-coupled orbitals and the spin-coupling coefficients are optimized simultaneously. Goddard et al. [56,57] have proposed the generalized valence bond (GVB) method. GVB has the advantage of compactness, as the wave functions are generally assumed to be formally purely covalent. However, GVB does not offer the clear relationship between the wave function and the various Lewis structure. Hiberty et al. [58,59] have also developed a general VB method and discussed chemical reactivity and structure.

20.2.2.1 The CASVB method [50,51]

We have proposed two types of CASVB method. In one method the valence bond structures are constructed over *orthogonal* localized orbitals, and in the other the structures are written with *non-orthogonal* localized orbitals. These are henceforth referred as orthogonal CASVB and non-orthogonal CASVB, respectively.

The idea of CASVB is based on the fact that the densities of variational wave functions are invariant under the transformations which hold the variational space unchanged.

In the CASSCF case, a complete active space (CAS) is invariant under the linear transformation of active orbitals and also that of configuration state functions (CSFs).

One may re-define the active orbitals utilizing the invariance of the active orbital space. In the orthogonal CASVB method, the LMOs constructed by Boys' localization procedure are used; that is, active orbitals are transformed so as to have the minimum sum of r^2 expectation values. If the active orbitals are defined appropriately, the LMOs obtained nearly always turn out to be localized on a single atomic center with small localization tails on to neighboring atoms. In the non-orthogonal CASVB case, the atomic-like orbitals are constructed by Ruedenberg's projected localization procedure.

Let Ψ^{CASSCF} be a CASSCF wave function

$$\Psi^{\mathrm{CASSCF}} = \sum_i C_i \Phi_i^{\mathrm{CSF}}, \qquad \Phi_i^{\mathrm{CSF}} \equiv \Phi_i^{\mathrm{CSF}}(\{\varphi_i\}) \tag{45}$$

where Φ_i^{CSF} are the CSFs constructed by the orthogonal orbitals set $\{\varphi_i\}$ and C_i are the known CAS configuration interaction (CI) expansion coefficients. Similarly, one may define the CASVB function in terms of spin-paired functions as

$$\Psi^{\mathrm{CASVB}} = \sum_i \mathrm{A}_i \Phi_i^{\mathrm{VB}}, \qquad \Phi_i^{\mathrm{VB}} \equiv \Phi_i^{\mathrm{VB}}(\{\lambda_i\}) \tag{46}$$

where Φ_i^{VB} is are a spin-paired function constructed by LMOs. The spaces, spanned by $\{\Phi_i^{\mathrm{CSF}}\}$ and $\{\Phi_i^{\mathrm{VB}}\}$, are identical. Since Eqs. (45) and (46) are different expressions of the identical wave function, one may write

$$\sum_j \mathrm{A}_j \Phi_j^{\mathrm{VB}} = \sum_j C_j \Phi_j^{\mathrm{CSF}} \tag{47}$$

Multiplying Eqs. (45) and (46) by Φ_i^{CSF} and integrating the products, one has a linear equation

$$\sum_j \Omega_{ij} \mathrm{A}_j = C_i \qquad \text{with} \qquad \Omega_{ij} = \langle \Phi_i^{\mathrm{CSF}} | \Phi_j^{\mathrm{VB}} \rangle \tag{48}$$

whose dimension is equal to the dimension of CAS. Solving this linear equation, one obtains CASVB wave function Ψ^{CASVB}. In the orthogonal CASVB case, one can use the common set of (Boys') LMOs as $\{\varphi_i\}$ as well as $\{\lambda_i\}$ since the LMOs remain CASSCF MOs. In that case, the linear equation (48) is reduced to a set of linear equations for each *orbital* configuration, and the matrix Ω_{ij} for each linear equation becomes a triangular matrix depending only on spin configurations. The linear equation (48) can, therefore, be solved with ease, compared with the non-orthogonal CASVB case.

The occupation number (or weight) of a resonance structure is calculated with

$$n_i = A_i^* \sum_j S_{ij} A_j \tag{49}$$

where S_{ij} are overlaps between the structures i and j, defined by

$$S_{ij} = \langle \Phi_i^{\mathrm{VB}} | \Phi_j^{\mathrm{VB}} \rangle \tag{50}$$

and satisfies the normalization

$$\sum_i n_i = 1 \tag{51}$$

Note that the occupation number n_i could be negative because of the non-orthogonality of resonance structures.

20.2.2.2 Description of electronic structure of benzene

As an example, a CASVB description for benzene is given in Fig. 20.2. See Refs. [50,51] for the computational details. The CASVB affords a clear view of the wave functions for the various states. The excitation process is represented in VB theory in terms of the rearrangement of spin couplings and charge transfer. The former generates the covalent excited states and the latter gives rise to the ionic excited states, in which the covalent bond is broken and a new ionic bond is formed. Thus, the singly, doubly, etc. polar structures are generated from their respective *parent* ground state covalent (nonpolar), singly, etc., polar structures.

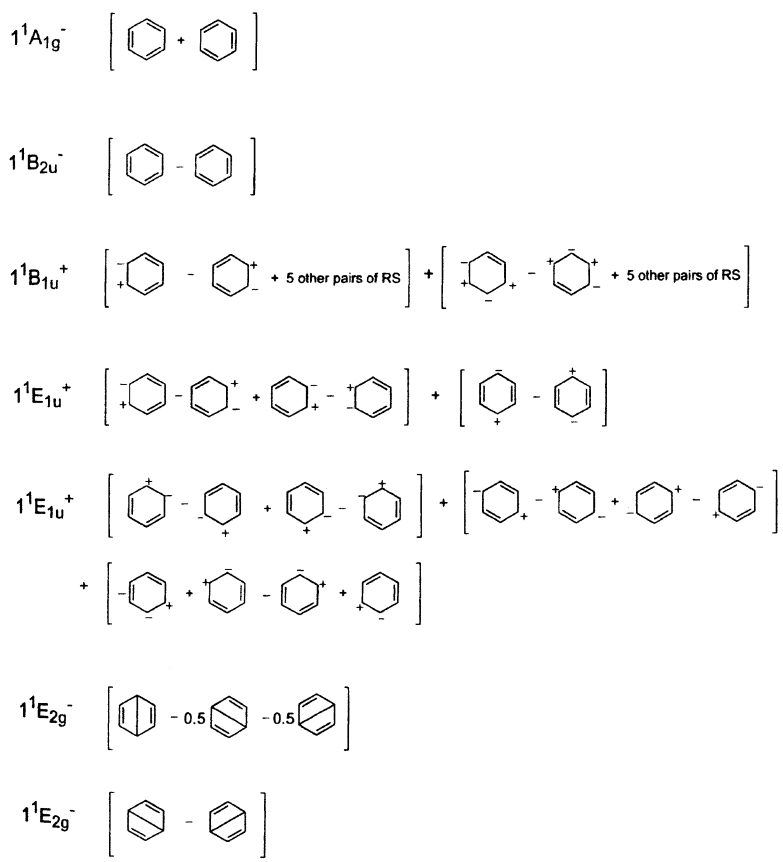

Fig. 20.2. CASVB description for the ground and $\pi \rightarrow \pi^*$ singlet excited states of benzene.

The ground state is represented by two covalent Kekulé structures as expected. The lowest excited $^1B_{2u}^-$ state is again described by a combination of the Kekulé structure. There are no significant contributions from the Dewar structures or the corresponding orthopolar structures. The linear combinations of the two equivalent Kekulé structures generate the plus and minus states. Their positive combination gives rise to the totally symmetric $^1A_{2g}^-$ ground state, while the negative combination yields the excited $^1B_{2u}^-$ state. The second and third $\pi \rightarrow \pi^*$ excited states are described by a number of ionic structures. There is no contribution from the covalent structures. The ionic character of these states can easily be found from a CASVB description. The highest valence excited states are the covalent $^1E_{2g}^-$ state. The state has a predominantly Dewar character with no contribution from the Kekulé structures. Thus, the Kekulé structures dominate the ground state and the singly excited $1B_{2u}^-$ state while the Dewar structures dominate the doubly excited degenerate $^1E_{2g}^-$ states. The states described by Dewar structures are described by doubly, triply, etc. excitations in an MO language.

20.2.2.3 Description of chemical reaction—hydrogen exchange reactions $H_2 + X \rightarrow H + HX$ (X = F, Cl, Br, and I) [60]

We examine a series of reactions including ionic bonds

$$H_2 + F \rightarrow H + HF \quad \text{(R1)}$$

$$H_2 + Cl \rightarrow H + HCl \quad \text{(R2)}$$

$$H_2 + Br \rightarrow H + HBr \quad \text{(R3)}$$

$$H_2 + I \rightarrow H + HI \quad \text{(R4)}$$

The reaction for fluorine (R1) is highly exothermic, while the reactions for chlorine (R2), bromine (R3), and iodine (R4) are endothermic. The heats of these reactions are 30.8, − 1.2, − 16.7, and − 32.7 kcal/mol for reactions (R1), (R2), (R3), and (R4), respectively. According to Hammond's postulate, reaction (R1) should have an early TS, and reactions (R2) and (R3) should have late TSs. What the electronic states are during these reactions, and how the CASVB method describes the electronic structure, are our interests in this section.

The active spaces were constructed by distributing three electrons in three orbitals consisting of $H_1(1s)$, $H_2(1s)$, and $X(2p\sigma)$, i.e. CAS(3,3). The dimension of the CAS is eight. According to this CAS, eight linearly independent VB structures

$$\varphi_{H_A}\varphi_{H_B}(\alpha\beta - \beta\alpha)\cdot\varphi_X\alpha, \qquad H_A - H_B\,\dot{X} \quad \text{(I)}$$

$$\varphi_{H_B}\varphi_{H_B}\alpha\beta\cdot\varphi_X\alpha, \qquad H_A^+\,{}^-H_B\,\dot{X} \quad \text{(II)}$$

$$\varphi_{H_A}\varphi_{H_A}\alpha\beta\cdot\varphi_X\alpha, \qquad H_A^-\,{}^+H_B\,\dot{X} \quad \text{(III)}$$

$$\varphi_{H_A}\alpha\cdot\varphi_{H_B}\varphi_X(\alpha\beta - \beta\alpha), \qquad \dot{H}_A\,H_B - X \quad \text{(IV)}$$

$$\varphi_{H_A}\alpha\cdot\varphi_{H_B}\varphi_{H_B}\alpha\beta, \qquad \dot{H}_A\,H_B^-\,{}^+X \quad \text{(V)}$$

$$\varphi_{H_A}\alpha\cdot\varphi_X\varphi_X\alpha\beta, \qquad \dot{H}_A\,H_B^+\,{}^-X \quad \text{(VI)}$$

$$\varphi_{H_B}\alpha\cdot\varphi_X\varphi_X\alpha\beta, \qquad H_A^+\,\dot{H}_B\,{}^-X \tag{VII}$$

and

$$\varphi_{H_A}\varphi_{H_A}\alpha\beta\cdot\varphi_{H_B}\alpha, \qquad H_A^-\,\dot{H}_B\,{}^+X \tag{VIII}$$

were used to construct CASVB functions, where the normalization constants and antisymmetrizers are omitted.

The contributions of the covalent H_AH_B bond, ionic H_AH_B bond, covalent H_BX bond, ionic H_BX bond, and ionic H_AX bond are defined by

$$n_{\text{Covalent } H_AH_B} = n_I, \qquad n_{\text{Ionic } H_AH_B} = n_{II} + n_{III} \tag{52}$$

$$n_{\text{Covalent } H_BX} = n_{IV}, \qquad n_{\text{Ionic } H_BX} = n_V + n_{VI} \tag{53}$$

and

$$n_{\text{Ionic } H_AX} = n_{VII} + n_{VIII} \tag{54}$$

Furthermore, the contributions of the total H_AH_B and H_BX bond structures are defined by the sums of the covalent structure (I)/(IV) and ionic structures (II)/(V) and (III)/(VI)

$$n_{H_AH_B} = n_{\text{Covalent } H_AH_B} + n_{\text{Ionic } H_AH_B}, \qquad n_{H_BX} = n_{\text{Covalent } H_BX} + n_{\text{Ionic } H_BX} \tag{55}$$

Let us first examine the electronic structure at the TS structure of the four reactions. Table 20.6 shows the VB structure at the TSs of $H_2 + X \rightarrow H + HX$. We can see that the covalent VB structures are dominant: the structures are well described by the superposition of the HH and HX covalent structure with small H^+H and H^+X^- ionic contributions. Using Eq. (55), these structures are further classified as the HH and HX bonds, as shown in Table 20.6. For X = F, the contribution of the HH bond (55.5%) is larger than that of the HX bond (39.4%). This relation is reversed for X = Cl, Br, and I. The contribution of the HH bond increases as the halogen atom becomes heavier (55.8 (Cl), 69.8 (Br), and 76.4% (I)). This means that *the TS of chemical bonds* (that is, the point where the occupation numbers of the two chemical bonds are equal) is placed in

Table 20.6 Occupation numbers of the VB structures at the TS

	H + H + F	H + H + Cl	H + H + Cl	H + H + Cl
H–H Ẋ (I)	0.485	0.328	0.217	0.172
$H^+\,{}^-H$ Ẋ (II)	0.053	0.059	0.043	0.034
$H^-\,{}^+H$ Ẋ (III)	0.017	−0.022	−0.023	−0.019
Ḣ H–X (IV)	0.252	0.385	0.514	0.591
Ḣ $H^-\,{}^+X$ (V)	−0.005	0.018	0.042	0.073
Ḣ $H^+\,{}^-X$ (VI)	0.147	0.155	0.142	0.100
H^-Ḣ ^+X (VII)	0.006	0.013	0.011	0.010
H^+Ḣ ^-X (VIII)	0.045	0.064	0.053	0.039
HH bond	0.555	0.365	0.237	0.187
HX bond	0.394	0.558	0.698	0.764
Others	0.051	0.077	0.064	0.049

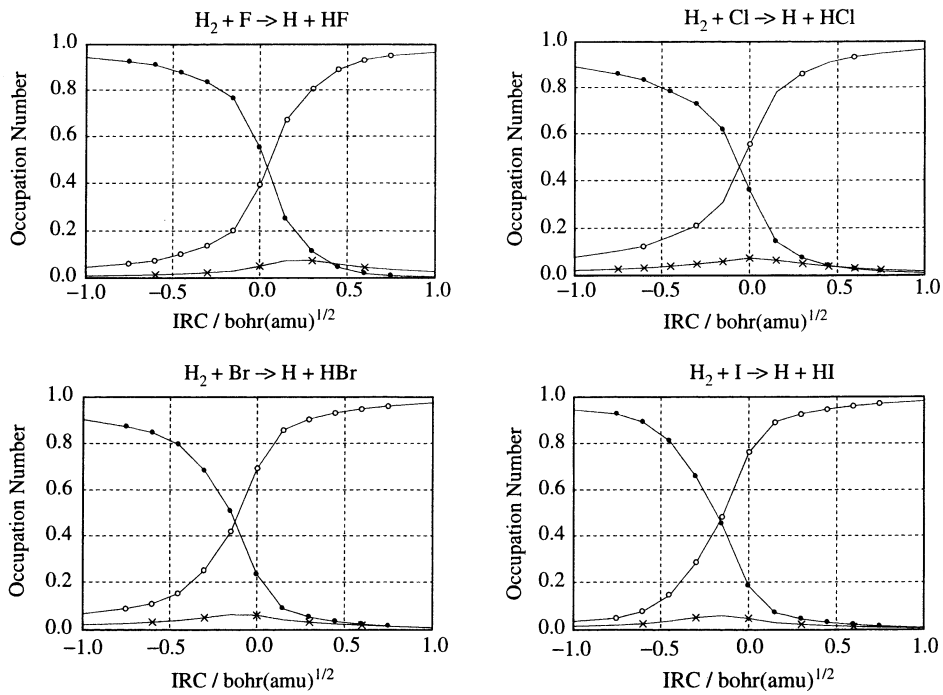

Fig. 20.3. Changes in the occupation numbers of the total HH bond (●), total HX bond (○), and the other (×) VB structures along IRC. The origin of the horizontal axis corresponds to the TS.

the reactant side in the X = F case and in the product side for the case of X = Cl, and it shifts more to the product side as the halogen atom becomes heavier.

We then examine the bond nature during the reactions. Fig. 20.3 shows the changes in the total occupation number of the HH and HX bond structures along the IRC. The occupation numbers of the HH and HX bond structures change rapidly and the curves cross near the TS. The crossing points are located at 0.07, −0.11, −0.25, and −0.33 bohr(a.m.u.)$^{1/2}$ for X = F, Cl, Br, and I, respectively, where a negative sign means the crossing point is located before the TS and a positive sign after the TS. We can see the trend that the crossing point shifts from the reactant side to the product side as the halogen atom gets heavier. The changes in the contents of the HH and HX bonds are plotted in Fig. 20.4. As expected in these reactions including ionic bonds, the contribution of ionic bond increases as that of the covalent bond increases. However, the crossing point of HH and HX covalent bonds are still close to that of the HH and HX bonds in Fig. 20.3. The covalent bonds are mainly responsible for determining the crossing points.

If we re-take *the TS of chemical bonds* as the origin, these facts well explain the shift of TS (from the early TS side to the late TS side) that Hammond's postulate predicts, indicating that the CASVB method is a powerful tool for describing the electronic structure and chemical bond during chemical reactions.

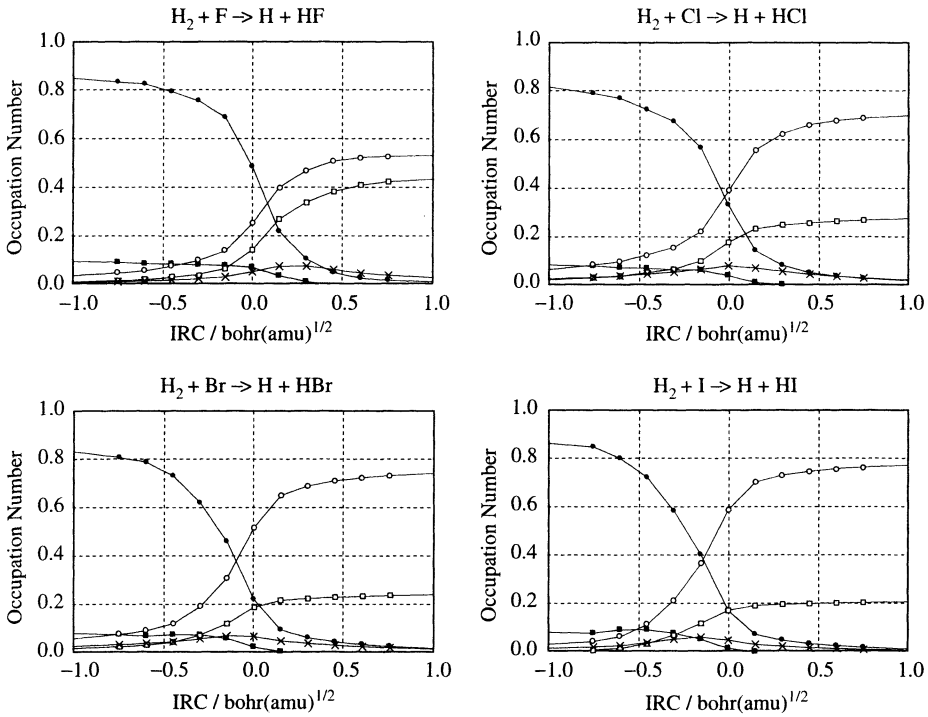

Fig. 20.4. Changes in the occupation numbers of the covalent HH bond (●), ionic HH bond (■), covalent HX bond (○), ionic HX bond (□), and the other (×) VB structures along the IRC.

20.3 LONG-RANGE AND OTHER CORRECTIONS FOR DENSITY FUNCTIONALS

20.3.1 Conventional correction schemes in density functional theory

In this century, the main concerns of theoretical chemistry obviously make the transition from accurate investigations of small molecules to the designs of complicated large molecular systems; e.g. proteins, nano-materials, environmental catalyses, and so forth. What is necessary for approaching these systems is an accurate theory of low-computational order. DFT [61–63] is expected to be a major candidate for such a theory at present, because this theory gives accurate chemical properties despite its low-computational order that may be reduced to order-N. In DFT, electronic states are usually determined by solving the nonlinear Kohn–Sham equation [61] with an exchange-correlation density functional. The most remarkable characteristic of DFT is the exchange-correlation energy part that is approximated by a one-electron potential functional. Hence, calculated DFT results depend on the form of this exchange-correlation functional.

In last two decades, various kinds of exchange functionals have been suggested especially for generalized gradient approximations (GGA) [64–67] beyond the local

density approximation (LDA) functional [68]. Due to the requirement of order, these GGA exchange functionals are usually expressed as a functional of $x_\sigma = |\nabla\rho_\sigma|/\rho_\sigma^{4/3}$, where ρ_σ is the electron density of spin σ and $\nabla\rho_\sigma$ is the gradient of the density [69]. What should be noticed is that most GGA exchange functionals have unique behaviors only for large x_σ [69,70]. This is because small-x_σ behaviors of functionals are restricted by the physical condition for slowly-varying density [71], although there is no definite conditions for rapidly varying density [67,69,70]. Hence, GGA exchange functionals are usually characterized by the behaviors for large-x_σ (i.e. low-density-high-gradient) density. Conventional exchange-correlation functionals will be discussed by Prof. Scuseria in this book. We will give a summary account of correction schemes for exchange functionals in this section.

Since the latter half of 1990s, hybrid functionals have appeared in DFT calculations. In hybrid functionals, (pure) GGA functionals are combined with the Hartree–Fock (HF) exchange integral at a constant rate. This idea may have come from an observation that DFT calculations using pure GGA functionals often give opposite errors to those in HF calculations. In 1993, Becke suggested hybrid B3LYP functional [72]. Based on a concept of adiabatic connection, B3LYP exchange-correlation energy are expressed by a combination of Becke 1988 (B88) exchange [64] and Lee–Yang–Parr (LYP) correlation [73] GGA functionals, Slater (S) exchange [68] and Vosko–Wilk–Nusair (VWN) correlation [74] LDA functionals, and the HF exchange integral with three parameters:

$$E_{xc}^{B3LYP} = a_0 E_x^{HF} + (1 - a_0)E_x^S + a_x E_x^{B88} + (1 - a_c)E_c^{VWN} + a_c E_c^{LYP} \qquad (56)$$

where E_x^A and E_c^B are exchange and correlation energies of A and B, and a_0, a_x, and a_c are 0.2, 0.72, and 0.81, respectively. Atomic units have been used ($\hbar = e^2 = m = 1$, energies are in hartree, and distances are in bohr). This adiabatic connection may have some incompatible parts; for example, parameters in B88 and LYP functionals were originally determined to reproduce exact exchange and correlation energies. Nevertheless, B3LYP becomes the most popular DFT functional in quantum chemistry, because it gives very accurate results for a wide variety of chemical properties. Becke 1997 (B97) [75] and Perdew–Burke–Ernzerhof 1996 (PBE0) [76] functionals are also hybrid functionals. Similar to B3LYP, these functionals combine GGA functionals with the HF exchange integral at a constant rate, and give accurate results for various chemical properties of molecules. However, inconsistencies in the adiabatic connection remains unsettled in these functionals.

Asymptotic corrections for exchange functionals have attracted attentions especially in time-dependent DFT (TDDFT) studies. In far regions from atomic nuclei, it is proved that exchange potential for σ-spin electrons, $v_{xc}^\sigma = \delta E_{xc}/\delta\rho_\sigma$ has the asymptotic relation [77]

$$\lim_{R\to\infty} v_{xc}^\sigma(\mathbf{R}) = -\frac{1}{R} \qquad (57)$$

where $R = |\mathbf{R}|$ and $\mathbf{R}$ is the distance vector from the nearest nucleus. On the ground of this relation, Van Leeuwen and Baerends suggested an exchange functional (LB) [78] by adapting the B88 exchange functional to the asymptotic behavior. Tozer and Handy suggested the asymptotic correction (AC) scheme that imposes, instead

of Eq. (57) [79,80]

$$\lim_{R\to\infty} v_{\mathrm{xc}}^{\sigma}(\mathbf{R}) = -\frac{1}{R} + \varepsilon_{\sigma}^{\mathrm{HOMO}} + I_{\sigma} \tag{58}$$

where $\varepsilon_{\sigma}^{\mathrm{HOMO}}$ is the eigenvalue of the highest occupied σ-spin molecular orbital and I_{σ} is the ionization potential of the σ-spin electron. It has been reported that underestimations of Rydberg excitation energies in TDDFT calculations are modified by using LB and AC schemes.

Besides, self-interaction correction (SIC) is one of the most popular correction schemes. Perdew and Zunger suggested a scheme for the application of SIC to occupied orbitals where the self-interaction components of the Coulomb and exchange energies are simply subtracted from the total exchange-correlation energy [81]

$$E_{\mathrm{xc}}^{\mathrm{SIC}}[\rho_{\alpha},\rho_{\beta}] = E_{\mathrm{xc}}[\rho_{\alpha},\rho_{\beta}] - \sum_{i,\sigma}\left(\frac{1}{2}\int \frac{\rho_{i\sigma}(\mathbf{R})\rho_{i\sigma}(\mathbf{R}')}{|\mathbf{R}-\mathbf{R}'|}\mathrm{d}^3\mathbf{R}\,\mathrm{d}^3\mathbf{R}' + E_{\mathrm{xc}}[\rho_{i\sigma},0]\right) \tag{59}$$

and potential

$$v_{\mathrm{xc}}^{i\sigma,\mathrm{SIC}}(\mathbf{R}) = \frac{\delta E_{\mathrm{xc}}^{\mathrm{SIC}}}{\delta\rho_{i\sigma}(\mathbf{R})} = \frac{\delta E_{\mathrm{xc}}[\rho_{\alpha},\rho_{\beta}]}{\delta\rho_{i\sigma}(\mathbf{R})} - \int \frac{\rho_{i\sigma}(\mathbf{R}')}{|\mathbf{R}-\mathbf{R}'|}\mathrm{d}^3\mathbf{R}' - \frac{\delta E_{\mathrm{xc}}[\rho_{i\sigma},0]}{\delta\rho_{i\sigma}(\mathbf{R})} \tag{60}$$

where $\rho_{i\sigma}$ is the ith orbital component of ρ_{σ}. This SIC scheme has been frequently used in energy band calculations of solid states for improving underestimated band gap energies. However, this scheme essentially requires an orbital-localization process [82] or transformation of functionals to an orbital-dependent form [83] due to the degrees of freedom in unitary transformations of orbitals. Tsuneda, Kamiya, and Hirao suggested a regional self-interaction correction (RSIC) scheme as a simple SIC method requiring no additional processes [84]. On the ground that total kinetic energy density, $\tau_{\sigma}^{\mathrm{total}} = \sum_{i}^{\mathrm{occ}} |\nabla\psi_{i\sigma}|^2$, approaches the Weizsäcker kinetic energy density, $\tau_{\sigma}^{\mathrm{W}} = |\nabla\rho_{\sigma}|^2/(4\rho_{\sigma})$ for self-interacted electrons, an exchange functional is spatially replaced with a self-interaction energy density only for regions, where $\tau_{\sigma}^{\mathrm{total}}$ approaches $\tau_{\sigma}^{\mathrm{W}}$, in this scheme. As the self-interaction energy density, exact exchange self-interaction energy densities of 1s orbitals in hydrogen-like atoms, $\psi_{i\sigma}^{1\mathrm{s}} = \sqrt{\alpha^3/\pi}\exp(-\alpha R)$, is employed such as

$$\varepsilon_{\mathrm{x}\sigma}^{\mathrm{RSIC}} = -\left(\frac{\rho_{\sigma}}{2R}\right)[1 - (1+\alpha R)\exp(-2\alpha R)] \tag{61}$$

where ε_{σ} is defined by $E_{\mathrm{x}} \equiv \sum_{\sigma}\int \varepsilon_{\mathrm{x}\sigma}\,\mathrm{d}^3\mathbf{R}$ and $\alpha = \nabla\rho_{\sigma}/(2\rho_{\sigma})$. By applying the RSIC scheme to chemical reaction calculations, it was found that underestimated barrier energies of pure functionals were clearly improved for some reactions.

As mentioned above, various correction schemes have been developed up to the present. However, there is room for further improvement in conventional correction schemes. Conventional hybrid functionals give poor excitation energies in TDDFT calculations as mentioned later. Asymptotic and SICs have little (or worse) effect on reproducibilities of molecular chemical properties. Recently, it has been proved that a long-range correction for exchange functionals obviously brings solutions to various

DFT problems that have never been solved by other functionals or corrections. In later sections, we will briefly review the background of the long-range correction scheme and will reveal the applicabilities of this scheme.

20.3.2 Long-range correction schemes for exchange functionals

Pure DFT exchange-correlation functionals have been represented by using only local quantities at a reference point: e.g. electron density, gradient of density, and etc. (We are now describing 'local' quantity as a quantity determined at a reference point for clarity, although gradient of density is known as a 'nonlocal' quantity in common use.) It is, therefore, presumed that pure functionals overestimate local contributions and underestimate nonlocal contributions. The most significant nonlocal contribution neglected in pure functionals may be the long-range electron–electron exchange interaction, because it may be impossible to represent this interaction as a functional of a one-electron quantity.

In 1996, Savin suggested a long-range exchange correction scheme for LDA functional [85]. In this scheme, the two-electron operator, $1/r_{12}$, is separated into the short-range and long-range parts naturally by using the standard error function erf such that

$$\frac{1}{r_{12}} = \frac{1 - \mathrm{erf}(\mu r_{12})}{r_{12}} + \frac{\mathrm{erf}(\mu r_{12})}{r_{12}} \tag{62}$$

where $r_{12} = |\mathbf{r}_1 - \mathbf{r}_2|$ for coordinate vectors of electrons, $\mathbf{r}_1$ and $\mathbf{r}_2$, and μ is a parameter that determines the ratio of these parts. Based on Eq. (62), the long-range exchange interaction is described by the HF exchange integral

$$E_{\mathrm{x}}^{\mathrm{lr}} = -\frac{1}{2}\sum_{\sigma}\sum_{i}^{\mathrm{occ}}\sum_{j}^{\mathrm{occ}}\int\int \psi_{i\sigma}^{*}(\mathbf{r}_1)\psi_{j\sigma}^{*}(\mathbf{r}_2)\frac{\mathrm{erf}(\mu r_{12})}{r_{12}}\psi_{j\sigma}(\mathbf{r}_1)\psi_{i\sigma}(\mathbf{r}_2)\mathrm{d}^3\mathbf{r}_1\,\mathrm{d}^3\mathbf{r}_2 \tag{63}$$

where $\psi_{i\sigma}$ is the ith σ-spin orthonormal molecular orbital. The LDA exchange functional is applied to the short-range exchange interaction such that

$$\begin{aligned} E_{\mathrm{x}}^{\mathrm{sr}} = &-\frac{3}{2}\left(\frac{3}{4\pi}\right)^{1/3}\sum_{\sigma}\int \rho_{\sigma}^{4/3}\left\{1 - \frac{8}{3}a_{\sigma}\left[\sqrt{\pi}\,\mathrm{erf}\left(\frac{1}{2a_{\sigma}}\right)\right.\right. \\ &\left.\left.+\left(2a_{\sigma} - 4a_{\sigma}^3\right)\exp\left(-\frac{1}{4a_{\sigma}}\right) - 3a_{\sigma} + 4a_{\sigma}^3\right]\right\}\mathrm{d}^3\mathbf{R} \end{aligned} \tag{64}$$

where $a_{\sigma} = \mu/(2k_{\sigma})$. The averaged relative momentum k_{σ} is written for LDA as the Fermi momentum, i.e. $k_{\mathrm{F}\sigma} = (6\pi^2\rho_{\sigma})^{1/3}$. Eq. (64) is derived by using the density matrix form corresponding to the LDA exchange functional

$$P_{1\sigma}^{\mathrm{LDA}}\left(\mathbf{R} + \frac{\mathbf{r}}{2}, \mathbf{R} - \frac{\mathbf{r}}{2}\right) = 3\frac{j_1(k_{\mathrm{F}\sigma}r)}{k_{\mathrm{F}\sigma}r}\rho_{\sigma}(\mathbf{R}) \tag{65}$$

where j_1 is the first-order spherical Bessel function.

However, Savin's scheme is inapplicable to conventional GGA exchange functionals, because GGA functionals usually have no corresponding density matrices unlike LDA. In 2001, Iikura et al. solved this problem by pushing gradient terms of GGA functionals into the momentum k_σ [86]. That is, the corresponding density matrix is determined for any GGA exchange functional by substituting $k_{F\sigma}$ in Eq. (65) with

$$k_\sigma^{GGA} = \left(\frac{9\pi}{K_\sigma^{GGA}}\right)^{1/2} \rho_\sigma^{1/3} \tag{66}$$

where K_σ^{GGA} is defined in an exchange functional used: $E_x^{GGA} = \int \rho_\sigma^{4/3} K_\sigma^{GGA}\, d^3\mathbf{R}$. Eq. (66) correctly reproduces the Fermi momentum $k_{F\sigma}$ for K_σ^{LDA}. By using k_σ^{GGA}, the short-range exchange energy in Eq. (64) is substituted by

$$E_x^{sr} = -\frac{3}{2}\left(\frac{3}{4\pi}\right)^{1/3} \sum_\sigma \int \rho_\sigma^{4/3} K_\sigma^{GGA} \left\{1 - \frac{8}{3} a_\sigma \left[\sqrt{\pi}\,\mathrm{erf}\left(\frac{1}{2a_\sigma}\right) + (2a_\sigma - 4a_\sigma^3)\exp\left(-\frac{1}{4a_\sigma}\right) - 3a_\sigma + 4a_\sigma^3\right]\right\} d^3\mathbf{R} \tag{67}$$

It is easily confirmed that Eq. (67) reproduces the original GGA exchange functional for $\mu = 0$. Parameter μ is determined to optimize bond distances of homonuclear diatomic molecules up to the third period as $\mu = 0.33$. This scheme is called 'long-range correction (LC) scheme'. The applicabilities of the LC scheme will be discussed in the later section.

Besides the LC scheme, we should mention the screened Coulomb potential hybrid functional as an attempt to take account of the long-range exchange effect. Heyd et al. developed this functional by dividing the exchange terms of the hybrid PBE0 functional into short- and long-range parts and by omitting a part of long-range exchange term as [87]

$$E_{xc}^{\omega PBEh} = aE_x^{HF,sr}(\omega) + (1-a)E_x^{PBE,sr}(\omega) + E_x^{PBE,lr}(\omega) + E_c^{PBE} \tag{68}$$

where $a = 1/4$ is a mixing coefficient and ω is an adjustable parameter. The main characteristics of this functional are the inclusion of the short-range HF exchange integral and the exclusion of the long-range HF exchange integral. This functional gives more accurate chemical properties than those of B3LYP for G2 and G3 set of molecules [87,88]. It is, however, presumed that this functional may not solve DFT problems arising from the lack of long-range exchange effects due to the exclusion of the long-range HF exchange integral. Moreover, Leininger et al. extended the above Savin's scheme by using the long-range exchange integral for the multireference configuration interaction (MRCI) wavefunction [89]. Electron correlations in long-range interactions may hardly affect calculated properties of standard molecules. However, electron correlations may be important for the comparison of molecules that have much different spin-multiplicity or neardegeneracy.

20.3.3 Applicabilities of long-range correction scheme

In this section, the LC scheme are examined by illustrating its applicabilities to three DFT problems that have never been solved: (1) poor reproducibilities of van der Waals (vdW)

bondings, (2) underestimations of Rydberg excitation energies, oscillator strengths, and charge transfer excitation energies in time-dependent density functional calculations, and (3) systematic overestimations of atomization energies of transition metal dimers.

20.3.3.1 Van der Waals calculations

One of the most critical DFT problems is the poor reproducibility of vdW bondings. Actually, conventional correlation functionals have incorporated no vdW interactions. Since vdW bondings, however, often determine structures of large-scale molecules, accurate calculations of vdW bondings are a pressing problem in DFT. Several DFT studies have been made on vdW calculations by using, e.g. a perturbation theory based on DFT [90]. The most effective and general way may be the use of a vdW functional. Up to the present, various types of vdW functionals have been suggested [91–93]. Some of these functionals reproduce accurate vdW C_6 coefficient comparable to the results of high-level *ab initio* methods [91]. However, these functionals give poor vdW bondings of, e.g. rare gas dimmers by simply combining with a conventional exchange-correlation functional in DFT calculations. It is presumed that this problem may be due to the lack of long-range interactions in exchange functionals, because vdW bondings are supposed to be in the balance between vdW attraction and long-range exchange repulsion interactions. On this ground, Kamiya et al. applied the LC scheme with a vdW functional to calculations of dissociation potentials of rare-gas dimmers [94]. Andersson–Langreth–Lundqvist (ALL) functional was used as the vdW functional [91]. This functional was developed to be correct for both separated electron gas regions and far-apart atoms. In this functional, a damping factor was used to diminish the vdW energy for regions at a short distances.

In Fig. 20.5, calculated dissociation potential energy curves of Ar_2 are shown for pure GGA functionals (BOP and PBEOP) [95] and LC functionals (LC-BOP and LC-PBEOP) with no vdW functionals. The 6-311++G(3df,3pd) basis functions was used [96–98]. The basis set superposition error was corrected by a counterpoise method [99]. As the figure shows, LC functionals give very close potential curves to each other, although pure GGA functionals provide obviously different curves. This may indicate that a long-range correction is necessary for exchange functionals to reproduce vdW bondings.

Next, Fig. 20.6 displays calculated dissociation potentials of Ar_2 by LC-BOP + ALL and conventional sophisticated functionals (mPWPW91 [100], mPW1PW91 [100], and B3LYP + vdW [101]). The second-order Møller–Plesset perturbation (MP2) and experimentally predicted (Expt) [16] potential curves are also shown for comparison. The figure clearly shows that LC-BOP + ALL functional gives accurate vdW potential curve in comparison with the results of MP2 and other conventional DFTs. It is, therefore, necessary for accurate DFT calculations of vdW bondings to use both long-range-corrected exchange and vdw-incorporated correlation functionals.

20.3.3.2 Time-dependent density functional calculations

Time-dependent density functional theory (TDDFT) becomes widely used as a simple method for rapid and accurate calculations of molecular excitation energies. It has, however, been reported that conventional TDDFT calculations underestimate Rydberg excitation energies, oscillator strengths, and charge-transfer excitation energies.

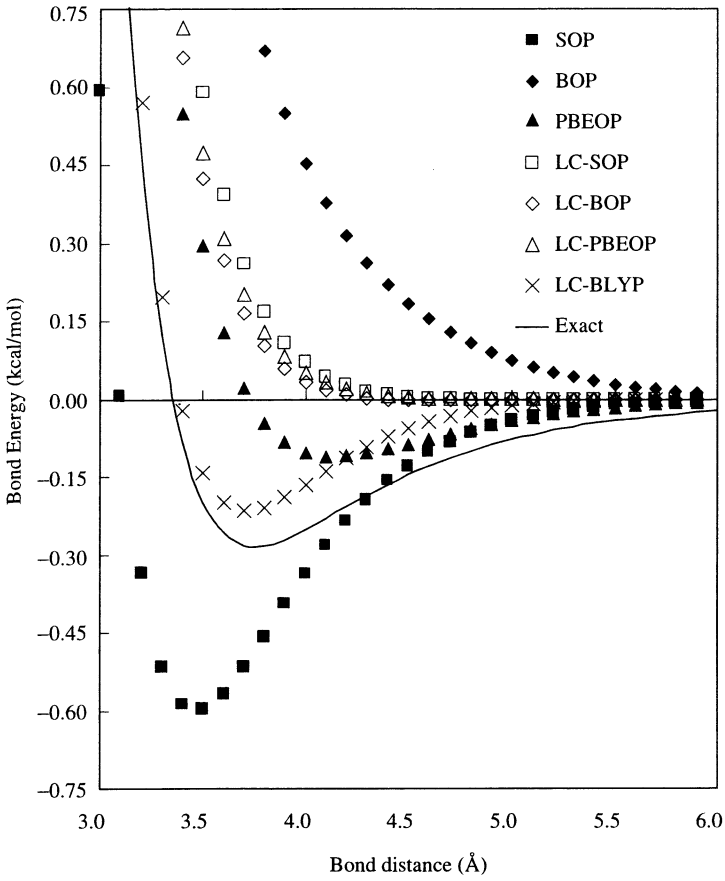

Fig. 20.5. Calculated bond energy potentials of argon dimer for long-range exchange corrected functionals (LC-SOP, LC-BOP, and LC-PBEOP). Pure functionals are also presented for comparison. Highly accurate potentials are also shown for comparison.

Tawada et al. supposed that this problem may also come from the lack of long-range exchange interaction, and applied the LC scheme to TDDFT calculations [102].

Table 20.7 summarizes mean absolute errors in calculated excitation energies of five typical molecules by TDDFT. The table also displays calculated results of asymptotically corrected AC [79] and LB [78] (AC-BOP and LBOP) and hybrid B3LYP [72] functionals, which are mentioned in the former section. The *ab initio* SAC-CI [103] results are also shown to confirm the accuracies. The 6-311G++(2d,2p) basis set was used in TDDFT calculations [104,105]. As the table indicates, the LC scheme clearly improves Rydberg excitation energies that are underestimated for pure BOP functional, at the same (or better) level as the AC scheme does. It should be noted that LC and AC schemes also provide improvements on valence excitation energies for all molecules. LC and AC results are comparable to SAC-CI results. The LB scheme clearly modifies

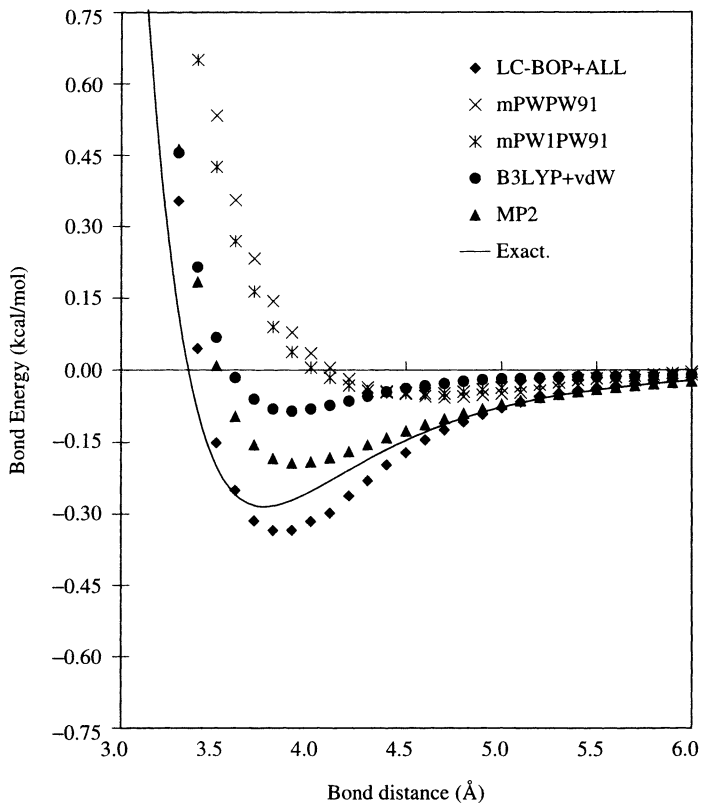

Fig. 20.6. Calculated bond energy potentials of argon dimer for LC-BOP+ALL functional. For comparison, calculated potentials of conventional sophisticated density functional schemes (mPWPW91, mPW1PW91, and B3LYP + vdW) and those of MP2 are also presented. Highly accurate potentials are also shown for comparison.

Rydberg excitation energies, and however brings underestimations of valence excitation energies. B3LYP results are obviously worse than LC and AC results for both valence and Rydberg excitation energies.

Next, calculated oscillator strengths of excited states by TDDFT are shown in Table 20.8. As is clearly shown in the table, LC scheme drastically improves oscillator strengths, which are underestimated for BOP as second to hundredth part of experimental values, to the same digit. Although AC-BOP, LBOP, and B3LYP also provide closer oscillator strengths to the experimental values than BOP do, the accuracies are unsatisfactory in comparison with LC-BOP ones. It is, therefore, concluded that the lack of long-range interactions in exchange functional may also cause the underestimations of oscillator strengths in TDDFT calculations.

Finally, calculated lowest charge transfer excitation energies of ethylene–tetrafluoroethylene dimer are shown in Fig. 20.7. Dreuw et al. recently suggested that poor charge transfer excitation energies of far-aparted molecules may be one of the main problems

Table 20.7 Mean absolute errors in calculated excitation energies of five typical molecules by TDDFT in eV

Molecule		LC-BOP	BOP	AC-BOP	LBOP	B3LYP	SAC-CI
N_2	Valence	0.36	0.40	0.27	1.48	0.54	0.33
	Rydberg	0.90	2.37	0.84	0.43	1.30	0.25
	Total	0.54	1.06	0.46	1.13	0.79	0.30
CO	Valence	0.19	0.28	0.17	1.02	0.36	0.26
	Rydberg	0.75	2.06	0.79	0.42	1.16	0.27
	Total	0.47	1.17	0.48	0.72	0.76	0.27
H_2CO	Valence	0.25	0.59	0.24	0.52	0.26	0.45
	Rydberg	0.47	1.66	0.59	0.07	0.84	0.13
	Total	0.40	1.30	0.47	0.22	0.64	0.24
C_2H_4	Valence	0.30	0.47	0.24	1.52	0.47	0.11
	Rydberg	0.18	1.41	0.58	0.69	0.92	0.17
	Total	0.20	1.28	0.53	0.80	0.85	0.16
C_6H_6	Valence	0.21	0.28	0.24	0.84	0.26	0.35
	Rydberg	0.24	1.01	0.88	0.35	0.56	0.15
	Total	0.23	0.74	0.64	0.53	0.44	0.22

of TDDFT [106]. They pointed out that intermolecular charge transfer excitation energies of far-aparted molecules should have the correct asymptotic behavior for long intermolecular distance. That is, for long molecular–molecular distances R and R_0 ($R > R_0$), charge transfer energy ω_{CT} should satisfy

$$\omega_{CT}(R) - \omega_{CT}(R_0) \geq -\frac{1}{R} + \frac{1}{R_0} \tag{69}$$

The figure shows that LC-BOP gives the correct asymptotic behavior as is different from AC-BOP and LBOP do. Although B3LYP recovers a part of this behavior, the degree is in proportion to the mixing rate of the HF exchange integral. Hence, this result may also indicate that problems in conventional TDDFT calculations come from the lack of long-range exchange interactions in exchange functionals rather than the poor far-nucleus asymptotic behavior of exchange functionals.

Table 20.8 Calculated oscillator strengths of excited states of typical molecules by TDDFT ($\times 10^{-2}$)

System	State	LC-BOP	BOP	AC-BOP	LBOP	B3LYP	SAC-CI	Exptl
N_2	$^1\Pi_u$	11.05	0.28	2.02	4.18	1.33	8.14	24.3
	$^1\Sigma_u^+$	24.06	0.69	6.07	3.60	3.84	15.67	27.9
CO	$^1\Pi$	19.76	8.66	6.68	5.97	11.24	9.63	17.6
H_2CO	$^1B_2$	2.19	1.68	1.02	3.02	2.71	1.88	4.13, 2.8, 3.8, 3.2
	$^1A_1$	6.94	2.11	2.62	1.80	3.64	4.26	6.05, 3.2, 3.8, 3.6
	$^1B_2$	6.50	1.75	2.42	2.23	2.32	2.95	2.81, 1.7, 1.9
C_2H_4	$^1B_{3u}$	12.85	3.49	4.77	5.08	6.75	8.20	4.00
	$^1B_{1u}$	73.85	12.85	24.41	32.38	34.67	40.65	29.00
C_6H_6	$1\,^1E_{1u}$	134.02	49.71	48.59	53.48	58.31	103.05	120, 90.0, 95.3

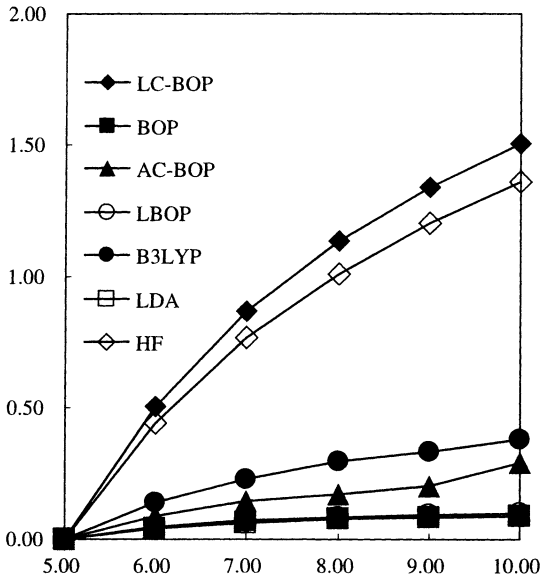

Fig. 20.7. The lowest charge transfer excitation energy of ethylene–tetrafluoroethylene dimer for the long intermolecular distance calculated by TDDFT employing various types of functionals. For all methods, the excitation energy at 5.0 Å is set to zero.

20.3.3.3 Transition metal dimer calculations

Yanagisawa et al. calculated the equilibrium geometries and the atomization energies for the first- to third-row transition metal dimers and concluded the following [107,108]:

1. Pure functionals tend to overstabilize electron configurations that contain orbitals in a high-angular momentum shell that is not fully occupied. This tendency is reduced from the first- to third-row transition metal dimers.
2. The overestimations of atomization energies of dimers are associated with the errors in outermost s–d interconfiguration transition energies of atoms. The latter errors may be due to the lack of long-range exchange interactions of outermost *s* and *d* orbitals that are fairly different in distributions. Hence, this lack may also cause the overestimations of the atomization energies.
3. B3LYP generally gives more accurate atomization energies than those of pure functionals, even if high-angular momentum orbitals are present in the configuration. However, B3LYP gives an erroneous energy gap between the configurations of fairly different spin-multiplicity probably due to the unbalance of the exchange and correlation functionals.

Based on this discussion, Tsuneda et al. applied the LC scheme to calculations of transition metal dimers [109].

Errors in calculated atomization energies of transition metal dimers are displayed in Fig. 20.8. The Wachters $+f$ basis set was used [110–112]. The figure shows that the LC scheme obviously improves the systematic overestimations calculated by pure

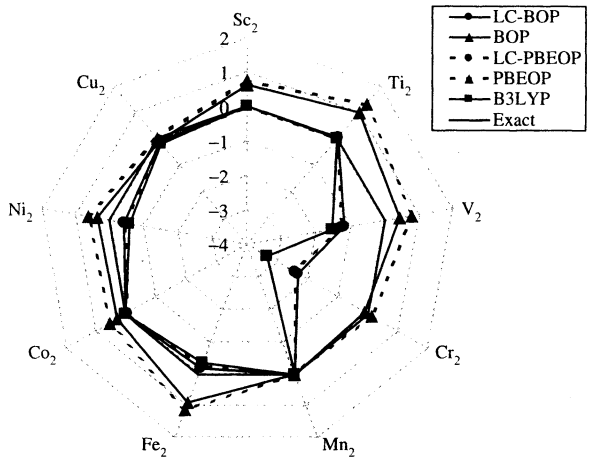

Fig. 20.8. Errors in calculated atomization energies of the first-row transition metal dimers for LC functionals (LC-BOP and LC-PBEOP), pure functionals (BOP and PBEOP), and B3LYP in eV. The line of no-error is also illustrated.

BOP functional. It was, therefore, proved that these overestimations maybe due to the lack of long-range exchange interactions in exchange functionals. It was also found that LC-BOP fairly underestimates the atomization energies of V_2 and Cr_2. As supposed from the similarity to B3LYP results, this underestimation may come from the errors in the HF exchange integral. That is, the HF exchange integral overstabilizes high-spin electronic states, because it only incorporates parallel-spin electron–electron interactions. It is, therefore, expected that this problem may be solved by taking well-balanced electron correlation into account for the long-range exchange part. The figure also shows that the LC scheme makes calculated atomization energies of different functionals much closer to each other. That is, the uniquenesses of functionals dissappeared after the long-range correction in this calculation. This may also support the conclusion that the lack of long-range exchange interactions is deeply committed to the overestimated atomization energies of dimers.

Table 20.9 Calculated barrier energies and bond distances of $H_2 + H \rightarrow H + H_2$ reaction

Molecule functional	Barrier height		Optimized geometry	
	Classical	ZPVC	$R(H_2)$	$R(H_3)$
LC-BOP	10.1	9.3	0.752	0.940
BOP	3.5	2.8	0.743	0.934
BLYP	2.9	2.2	0.745	0.930
B3LYP	4.3	3.5	0.742	0.934
Refs.	–	9.6	0.741	–

Barrier energies are in kcal/mol and optimized geometries are in Å. Reference values are the quantum Monte Carlo results.

Table 20.10 Calculated static isotropic polarizabilities by time-dependent Kohn–Sham theory in atomic unit

Molecule	LC-BOP	BOP	B3LYP	Exp.
Cl_2	30.87	31.69	31.16	30.35
CO_2	17.58	17.82	17.36	17.51
F_2	8.83	8.87	8.69	8.38
H_2O	10.03	10.49	9.95	9.64
H_2S	24.72	25.64	25.11	24.71
HCl	17.74	18.33	17.90	17.39
HF	5.99	6.17	5.83	5.60
N_2	11.99	12.07	11.88	11.74
SO_2	25.63	26.30	25.75	25.61

20.3.3.4 Other calculations

Besides the above-mentioned calculations, Tsuneda et al. are now applying the LC scheme to calculations of chemical reactions [113] and (hyper)polarizabilities [114]. We will exhibit some present works to show the wide applicabilities of this scheme.

First, calculated results of $H_2 + H \rightarrow H + H_2$ reaction are summarized in Table 20.9 [113]. The pV6Z basis set was used [115]. The table shows that the LC scheme remarkably improves underestimated reaction barrier energies of BOP. As far as we know, this result is certainly superior to results of other corrections that have ever reported. This may indicate that underestimations of reaction barriers in DFT calculations are also due to the lack of long-range interactions.

The LC scheme was also applied to overestimations of polarizabilities in DFT as shown in Table 20.10 [114]. The Sadlej valence triple zeta basis set was used [116,117]. The table shows that calculated polarizabilities of LC-BOP are obviously more accurate than those of BOP. Compared to B3LYP results, LC-BOP shows more improvements in many cases. Similar results were found in calculations of anisotropies and S_{-4} Cauchy moments of polarizabilities. Hence, we may say that these overestimations also come from the lack of long-range interactions in exchange functionals.

As mentioned above, the LC scheme was found to give better results for various chemical properties than the results of conventional corrections including hybrid functionals. For some properties, the LC scheme provided equivalent improvements in comparison with B3LYP. This may indicate that accurate B3LYP results may be due to the equivalency in the mixed HF exchange energy to the LC scheme, rather than the validity of the constant weight hybridization of the HF exchange. This argument may require further examination of the LC scheme.

20.4 RELATIVISTIC MOLECULAR THEORY

20.4.1 Introduction

The relativistic effect has been considered as an essential factor to figure out molecular structures, chemical activities, or various properties of heavy-element systems.

Recently many quantum chemists have dedicated a lot of efforts to the calculation and treatment of the electronic structures of polyatomic systems including heavy elements, which are involved in many interesting chemical and physical phenomena. They still present unique difficulties to the theoretical study. Until recently, the relativistic effect had ever been thought less important for chemical properties because the relativity appears primarily in the core electrons, which had been believed to be unlikely to affect chemically active valence regions dramatically. Recent studies, however, have revealed not only quantitatively but also qualitatively that the relativistic effect plays essential and comprehensive roles in total natures of molecular electronic structures for heavy-element systems. We are nowadays convinced that the relativistic effect is definitely important for the accurate theoretical treatment of heavy-element systems as well as the electron correlation effect.

To treat relativistic effects theoretically, the Dirac equation is usually solved rather than the non-relativistic Schrödinger equation. The one-electron Dirac Hamiltonian is written by

$$H_{\mathrm{D}} = c\boldsymbol{\alpha}\cdot\mathbf{p} + \beta c^2 + V_{\mathrm{ext}} \tag{70}$$

where the constant c is the speed of light, V_{ext} is the external potential, and $\mathbf{p}$ $(= -i\nabla)$ is the momentum operator. The 4×4 Dirac matrices $\boldsymbol{\alpha}$ and β in Eq. (70) are given by

$$\alpha_t \equiv \begin{pmatrix} 0_2 & \sigma_t \\ \sigma_t & 0_2 \end{pmatrix}, \qquad t = (x, y, z), \qquad \beta \equiv \begin{pmatrix} \mathbf{I}_2 & 0_2 \\ 0_2 & -\mathbf{I}_2 \end{pmatrix} \tag{71}$$

with the 2×2 Pauli spin matrices σ_t,

$$\sigma_x \equiv \begin{pmatrix} 0 & 1 \\ 1 & 0 \end{pmatrix}, \qquad \sigma_y \equiv \begin{pmatrix} 0 & -i \\ i & 0 \end{pmatrix}, \qquad \sigma_z \equiv \begin{pmatrix} 1 & 0 \\ 0 & -1 \end{pmatrix} \tag{72}$$

Since the Dirac equation is valid only for the one-electron system, the one-electron Dirac Hamiltonian has to be extended to the many-electron Hamiltonian in order to treat the chemically interesting many-electron systems. The straightforward way to construct the relativistic many-electron Hamiltonian is to augment the one-electron Dirac operator, Eq. (70) with the Coulomb or Breit (or its approximate Gaunt) operator as a two-electron term. This procedure yields the Dirac–Coulomb (DC) or Dirac–Coulomb–Breit (DCB) Hamiltonian derived from quantum electrodynamics (QED)

$$H = \sum_i H_{\mathrm{D}}(\mathbf{r}_i) + \sum_{i>j} g_{ij} \tag{73}$$

where

$$g_{ij}^{\mathrm{C}} = \frac{1}{r_{ij}} \tag{74}$$

and

$$g_{ij}^{\mathrm{CB}} = \frac{1}{r_{ij}} - \frac{1}{2}\left(\frac{(\alpha_i \cdot \alpha_j)}{r_{ij}} + \frac{(\alpha_i \cdot r_{ij})(\alpha_j \cdot r_{ij})}{r_{ij}^3}\right) \tag{75}$$

The DCB Hamiltonian is covariant to first order, and the presence of the Breit (or approximate Gaunt) interaction serves to increase the accuracy of calculated spectroscopic splittings and core binding energies.

Historically, approaches to treat the electronic structure relativistically have split into two camps: one is the four-component relativistic approach and another is the two-component one. Focusing on our recent studies, in this section, we will introduce these two types of relativistic approaches. The reader is referred to the detailed reviews for our recent relativistic works [118–120].

20.4.2 Four-component relativistic molecular theory

20.4.2.1 Dirac–Hartree–Fock and Dirac–Kohn–Sham methods

By an application of an independent-particle approximation with the DC or DCB Hamiltonian, the similar derivation of the non-relativistic Hartree–Fock (HF) method and Kohn–Sham (KS) DFT yields the four-component Dirac–Hartree–Fock (DHF) and Dirac–Kohn–Sham (DKS) methods with large- and small-component spinors.

The matrix DHF/DKS equation is generally written as

$$\mathbf{Fc} = \boldsymbol{\varepsilon}\mathbf{Sc} \tag{76}$$

where $\mathbf{c}$ is a matrix of molecular spinor coefficients, $\boldsymbol{\varepsilon}$ a spinor energy matrix, and $\mathbf{S}$ an overlap matrix

$$\mathbf{S}_{pq} = \begin{pmatrix} \mathbf{S}_{pq}^{\mathrm{LL}} & 0 \\ 0 & \mathbf{S}_{pq}^{\mathrm{SS}} \end{pmatrix} = \begin{pmatrix} \langle \chi_p^{\mathrm{L}} | \chi_q^{\mathrm{L}} \rangle & 0 \\ 0 & \langle \chi_p^{\mathrm{S}} | \chi_q^{\mathrm{S}} \rangle \end{pmatrix} \tag{77}$$

with two-component atomic spinors χ_p^{L} and χ_p^{S} for large (L) and small (S) components, respectively. Assuming the DC Hamiltonian, the Fock matrix $\mathbf{F}$ is given by

$$\begin{aligned} \mathbf{F}_{pq} &= \begin{pmatrix} \mathbf{F}_{pq}^{\mathrm{LL}} & \mathbf{F}_{pq}^{\mathrm{LS}} \\ \mathbf{F}_{pq}^{\mathrm{SL}} & \mathbf{F}_{pq}^{\mathrm{SS}} \end{pmatrix} \\ &= \begin{pmatrix} \mathbf{V}_{pq}^{\mathrm{LL}} + \mathbf{J}_{pq}^{\mathrm{LL}} - t_{\mathrm{ex}}\mathbf{K}_{pq}^{\mathrm{LL}} - t_{\mathrm{xc}}\mathbf{V}_{\mathrm{xc}pq}^{\mathrm{LL}} & c\boldsymbol{\Pi}_{pq}^{\mathrm{SL}} - t_{\mathrm{ex}}\mathbf{K}_{pq}^{\mathrm{SL}} \\ c\boldsymbol{\Pi}_{pq}^{\mathrm{LS}} - t_{\mathrm{ex}}\mathbf{K}_{pq}^{\mathrm{LS}} & \mathbf{V}_{pq}^{\mathrm{SS}} - 2c^2\mathbf{S}_{pq}^{\mathrm{SS}} + \mathbf{J}_{pq}^{\mathrm{SS}} - t_{\mathrm{ex}}\mathbf{K}_{pq}^{\mathrm{SS}} - t_{\mathrm{xc}}\mathbf{V}_{\mathrm{xc}pq}^{\mathrm{SS}} \end{pmatrix} \end{aligned} \tag{78}$$

Here, $\boldsymbol{\Pi}_{pq}^{\mathrm{X\bar{X}}}$, $\mathbf{V}_{pq}^{\mathrm{XX}}$, $\mathbf{V}_{\mathrm{xc}pq}^{\mathrm{XX}}$, $\mathbf{J}_{pq}^{\mathrm{XX}}$, and $\mathbf{K}_{pq}^{\mathrm{XY}}$ (X, Y = L or S, $\bar{\mathrm{L}}$ = S, and $\bar{\mathrm{S}}$ = L) are kinetic energy integral, electron–nuclear attraction integral, exchange-correlation potential,

Coulomb integral, and exchange integral matrices, respectively,

$$\mathbf{\Pi}_{pq}^{X\bar{X}} = \langle \chi_p^X | (\boldsymbol{\sigma}\cdot\mathbf{p}) | \chi_q^{\bar{X}} \rangle \tag{79}$$

$$\mathbf{V}_{pq}^{XX} = \langle \chi_p^X | V^{nuc} | \chi_q^X \rangle \tag{80}$$

$$\mathbf{V}_{xcpq}^{XX} = \left\langle \chi_p^X \middle| \frac{\delta E_{xc}}{\delta \rho} \middle| \chi_q^X \right\rangle \tag{81}$$

$$\mathbf{J}_{pq}^{XX} = \sum_{Y=L,S} \sum_{r,s} \mathbf{D}_{sr}^{YY} (\chi_p^X \chi_q^X | \chi_r^Y \chi_s^Y) \tag{82}$$

$$\mathbf{K}_{pq}^{XY} = \sum_{r,s} \mathbf{D}_{sr}^{XY} (\chi_p^X \chi_s^X | \chi_r^Y \chi_q^Y) \tag{83}$$

with the density matrix

$$\mathbf{D}_{sr}^{XY} = \sum_{i}^{N_{occ}} c_{si}^X c_{ri}^{Y^*} \tag{84}$$

The parameter t_{xc} is set to zero and one for the DHF and DKS approaches, respectively, and the constant t_{ex} is the parameter for the hybrid DFT approach, usually set to zero for the pure DFT approach.

The four-component DHF/DKS method is a theoretically straightforward relativistic approach. For heavy atoms four-component basis set expansion calculations are routine and attain spectroscopic accuracy together with extant correlation methods [121,122]. Recently the molecular DHF and DKS methods have become familiar and powerful relativistic approaches with the continuous development of efficient computational algorithms using the basis set expansion. Several four-component *ab initio* molecular orbital programs for polyatomics, e.g. MOLFDIR [123], DIRAC [124], BERTHA [125], and others [126–128], have been developed so far. Unfortunately, however, the treatment of more than one heavy atom within a molecule is not yet routine. The bottleneck in four-component calculations on heavy-element systems is evaluation of the two-electron electron repulsion integrals (ERIs). The number of relativistic integrals is greater than that of non-relativistic ones because the kinetic balance [129] between the large- and small-component primitive GTSs must be incorporated.

We have recently developed an efficient computational scheme for the four-component method that employs four-component contraction for molecular basis spinors and the new atomic spinor (AS) integral algorithm [130–132]. In the following sections we will briefly introduce our new relativistic scheme.

20.4.2.2 *Generally contracted Gaussian-type spinors and kinetic balance*

Accurate treatment of core spinors and of the valence spinors in the core region by a large basis set expansion is necessary, because most major relativistic effects, or the kinematic

effects, come from the region near the nuclei. Because the core changes little with chemical environment, the extensive basis set contraction is possible. The difficulty in introducing contracted GTSs lies in the fact that the kinetic balance condition [129] between the large- and small-component primitive GTSs and spin–orbit splitting of spinors must be incorporated.

In our four-component molecular approach, thus, we use spin-coupled, kinetically balanced, generally contracted Gaussian-type spinors (GTSs) as basis functions. The basis expansion is

$$\begin{pmatrix} \psi_i^{2L} \\ \psi_i^{2S} \end{pmatrix} = \sum_{\mu}^{n} \begin{pmatrix} c_{\mu i}^{L} \varphi_{\mu}^{2L} \\ c_{\mu i}^{S} \varphi_{\mu}^{2S} \end{pmatrix} \tag{85}$$

where φ_{μ}^{2L} and φ_{μ}^{2S} are two-component basis spinors, and c_{μ}^{L} and c_{μ}^{S} are expansion coefficients. In Eq. (85), both scalar wavefunctions within a two-component basis spinor are multiplied by a common coefficient, thus, the dimensions of both the large and small components are n and the total number of variational parameters is $2n$. In the pioneering four-component program package, MOLFDIR, as well as in DIRAC, four-spinors are expanded in decoupled scalar spin-orbitals

$$\psi_i = \sum_{\mu}^{n^L} c_{\mu i}^{L\alpha} \varphi_{\mu}^{L\alpha} \begin{pmatrix} 1 \\ 0 \\ 0 \\ 0 \end{pmatrix} + \sum_{\mu}^{n^L} c_{\mu i}^{L\beta} \varphi_{\mu}^{L\beta} \begin{pmatrix} 0 \\ 1 \\ 0 \\ 0 \end{pmatrix} + \sum_{\mu}^{n^S} c_{\mu i}^{S\alpha} \varphi_{\mu}^{S\alpha} \begin{pmatrix} 0 \\ 0 \\ 1 \\ 0 \end{pmatrix} + \sum_{\mu}^{n^S} c_{\mu i}^{S\beta} \varphi_{\mu}^{S\beta} \begin{pmatrix} 0 \\ 0 \\ 0 \\ 1 \end{pmatrix} \tag{86}$$

There are $2n^L$ large-component and $2n^S$ small-component basis spinors. Imposing the kinetic balance implies that $2n^S > n = 2n^L$. Our scheme thus reduces the number of functions required for the small component.

The form of the large-component primitive set ψ_k^{2L} is chosen from large-component spinors obtained by analytical solution of the one-electron Dirac equation. The small-component set ψ_k^{2S} is derived so that it satisfies the accurate and rigorous kinetic balance condition *versus* ψ_k^{2L},

$$\psi_k^{2S} = i(V - E - 2c^2)^{-1}(\boldsymbol{\sigma}\cdot\mathbf{p})\psi_k^{2L} \tag{87}$$

rather than the condition

$$\psi_k^{2S} = i(\boldsymbol{\sigma}\cdot\mathbf{p})\psi_k^{2L} \tag{88}$$

20.4.2.3 Efficient evaluation of electron repulsion integrals

In construction of Coulomb and exchange integral matrices (Eqs. (82) and (83)), three types of ERIs, (LL|LL), (LL|SS) (or (SS|LL)), and (SS|SS), are required within the Coulomb approximation to the electron–electron interaction. Evaluation of ERIs

Table 20.11 CPU times (in hours) for computing four-component ERIs for Au_2, where the basis set used for Au is [19s14p10d5f]/(6s4p3d1f), which is commonly contracted between A = + and A = −

	LLLL + LLSS + SSSS	LLLL + LLSS	LLLL
Present[a]	1.37	0.77	0.21
DIRAC[b]	2.09	0.62	0.050
MOLFDIR[c]	76.35	21.16	1.63

[a]Number of basis spinors: 160 (for the large and small components).
[b]Number of basis spinors: 184 (for the large component) and 424 (for the small component).
[c]Number of basis spinors: 160 (for the large component) and 420 (for the small component).

includes a scaling with the forth power of the number of basis functions formally and is the most time-consuming step within the DHF/DKS calculation. To evaluate relativistic ERIs efficiently, we have recently developed a new integral evaluation method specialized for relativistic contracted GTSs [130,132]. The algorithm exploits the transfer relation of Head–Gordon and Pople (HGP) [133] and the accompanying coordinate expansion (ACE) formulas derived by Ishida [134] in the non-relativistic case. In this method, four-component ERIs (LL|LL), (LL|SS), and (SS|SS) reduce to several common two-center terms using the HGP transfer relation. The common integrals are evaluated rapidly using the ACE method.

We have performed comparative calculations of ERIs using MOLFDIR2000 and DIRAC version 3.2 in comparison with our REL4D program. MOLFDIR and DIRAC do not treat separately contracted REL4D-type basis sets. To make direct comparison possible, calculations with REL4D were done with the commonly contracted basis spinors employed in MOLFDIR and DIRAC, although the program is not optimized for such basis sets. Table 20.11 displays CPU times for computations on Au_2 with the [19s14p10d5f]/(6s4p3d1f) set. REL4D proved fastest for LLLL + LLSS + SSSS. LLLL + LLSS calculations with the present code were comparable to those of DIRAC. In the LLLL calculations, the present code worked about four times slower than DIRAC. Note that the numbers of spinors generated are different for each program: 160 for the large and small components in REL4D; 160 for the large component and 420 for the small component in MOLFDIR; 184 for the large component and 424 for the small component in DIRAC. The slightly larger basis size in DIRAC is caused by the fact that it uses, not spherical harmonic GTSs, but contracted Cartesian GTSs. This feature improves DIRAC's performance in some cases because the transformation from Cartesian to spherical harmonic is omitted. The reduced size of the small component basis renders our computational scheme efficient in storage, computation, and transformation of integrals, and in matrix manipulations.

20.4.2.4 *Relativistic pseudospectral approach*

Recently we have proposed more efficient relativistic molecular theory by an application of the pseudospectral (PS) approach [135]. In the PS approach [136,137], we use the mixed basis function between a grid representation in the physical space and spectral representation in the function space.

In the relativistic PS approach, the Coulomb matrix element (Eq. (82)) is given as

$$\mathbf{J}_{pq}^{XX} = \sum_{Y=L,S} \sum_{r,s} \mathbf{D}_{sr}^{YY} (\chi_p^X \chi_q^X | \chi_r^Y \chi_s^Y) \cong \sum_g^M w_g A_{pq}^{XX}(g) \sum_Y^{L,S} \left(\sum_r^N \sum_s^N D_{rs}^{YY} \chi_r^{Y^*}(g) \chi_s^Y(g) \right)$$

$$\equiv \sum_g^M w_g A_{pq}^{XX}(g) \rho(g) \tag{89}$$

with the three-center one-electron integral

$$A_{pq}^{XY}(g) = \int \chi_p^{X^*}(1) \frac{1}{|r_1 - r_g|} \chi_q^Y(1) dr_1 \tag{90}$$

and $\rho(g)$ is the electronic density, which is calculated in terms of the density matrix and atomic spinors at a coordinate r_g. Likewise, the exchange contribution in the relativistic PS approach is given as

$$\mathbf{K}_{pq}^{XX} = \sum_{r,s} \mathbf{D}_{sr}^{XX} (\chi_p^X \chi_s^X | \chi_r^X \chi_q^X) \cong \sum_g^M w_g \chi_p^{X^*}(g) \left[\sum_r^N \left(\sum_s^N D_{rs}^{XX} \chi_s^X(g) \right) A_{rq}^{XX}(g) \right] \tag{91}$$

and

$$\mathbf{K}_{pq}^{X\bar{X}} = \sum_{r,s} \mathbf{D}_{sr}^{X\bar{X}} (\chi_p^X \chi_s^X | \chi_r^{\bar{X}} \chi_q^{\bar{X}}) \cong \sum_g^M w_g \chi_p^{X^*}(g) \left[\sum_r^N \left(\sum_s^N D_{rs}^{\bar{X}X} \chi_s^X(g) \right) A_{rq}^{\bar{X}\bar{X}}(g) \right] \tag{92}$$

for diagonal (LL and SS) and non-diagonal (LS and SL) parts in the DHF or DKS matrix, respectively. We note that no non-diagonal three-center one-electron integral is required in construction of both Coulomb and HF-exchange matrix elements within the DC approximation. Only diagonal $A_{pq}^{LL}(g)$ and $A_{pq}^{SS}(g)$ integrals are required. The high efficiency is hence achieved in the relativistic PS approach.

The features of the relativistic PS-DHF/DKS method are as follows:

(1) The computational scaling is reduced from $O(N^4)$ to $O(N^3)$ (N; the number of basis sets).
(2) Since the PS evaluation of HF-exchange matrix elements as well as Coulomb ones is efficient, post HF methods and hybrid-type DFT are applicable.
(3) It is possible to treat the large molecular systems that are compact and three-dimensional with high-quality basis sets in contrast to the fast multipole moment (FMM) method.
(4) The multigrid technique can powerfully save considerable CPU time in the direct SCF procedure.
(5) The PS program code is parallelized efficiently because of adoption of the numerical grid partition.

(6) It is possible to obtain the numerical result with arbitrary accuracy at adequate CPU time by careful choice of the number of grid points.

Table 20.12 shows the spectroscopic constants and total energies of the gold dimer calculated with the relativistic PS-DFT method using three types of grids. The details of computations are given in Ref. [135]. The results obtained by the conventional DFT method with the analytical ERIs and the experimental data [138,139] are also listed for comparison. The PS results for spectroscopic constants and total energies become closer to the analytical results as the level of grids is improved. The relativistic PS-DFT method with the ultrafine grid, the highest level of grid sets in this study, gives excellent good agreement with the analytical result. For the equilibrium bond length and the harmonic frequency for Au_2, the deviation of the ultrafine PS result from the analytical one is negligibly small. The discrepancies of the dissociation energy and the total energy between ultrafine PS and analytical results are $\Delta D_e = -0.4$ eV and $\Delta E = 0.0098$ a.u., respectively. It is also found that the fine grid yields satisfactory results; the difference of the equilibrium bond length, the harmonic frequency, the dissociation energy, and the total energy between fine PS and analytical results are $\Delta R_e = 0.005$ Å, $\Delta\omega_e = 1$ cm^{-1}, $\Delta D_e = 0.3$ eV, and $\Delta E = 0.0376$ a.u., respectively.

The multigrid technique can be used in the SCF procedure of present PS calculations. This technique realizes the faster SCF calculation with the PS method. Average CPU times per one cycle for the direct SCF step in the DFT calculation including the ERI evaluation, the KS matrix construction, and the SCF diagonalization are also listed in Table 20.12. These times are taken from each single-point calculation at $R = 4.8$ a.u. In the present multigrid calculation, the coarse and medium grids are used in the first and second SCF stages, respectively. By adoption of the multigrid approach in this system, the PS methods with medium, fine, and ultrafine grids are 19, 13, and 9 times faster than the traditional analytical method, respectively.

Other PS applications to molecular systems also show that the relativistic PS-DHF/DKS approach is more efficient than the traditional approach without a loss of accuracy.

Table 20.12 Spectroscopic constants of the Au dimer calculated by conventional DFT and PS-DFT (B3LYP)

	Analytical	PS (medium)[a]	PS (fine)[b]	PS (ultra)[c]	Exptl
R_e (Å)	2.554	2.526	2.549	2.554	2.472
ω_e (cm^{-1})	168	191	169	168	191
D_e (eV)	1.98	2.11	2.01	1.94	2.36
Energy (a.u.)[d]	−0.7302	−0.8075	−0.7678	−0.7400	–
Time (s)[e]	17497	927	1352	1979	–

[a]Medium grid: 50 × 110 = 5500/atom.
[b]Fine grid: 75 × 194 = 14550/atom.
[c]Ultrafine grid: 96 × 302 = 28992/atom.
[d]Total DFT energy: −38096 a.u.
[e]Average CPU time per one cycle for the direct SCF step in the DFT calculation including the ERI evaluation, the KS matrix construction, and the SCF diagonalization.

20.4.3 Two-component relativistic molecular theory

20.4.3.1 Approximate relativistic Hamiltonians

Despite recent implementations of an efficient algorithm for the four-component relativistic approach, the DC(B) equation with the four-component spinors composed of the large (upper) and small (lower) components still demands severe computational efforts to solve, and its applications to molecules are currently limited to small- to medium-sized systems. As an alternative approach, several two-component quasi-relativistic approximations have been proposed and applied to chemically interesting systems containing heavy elements, instead of explicitly solving the four-component relativistic equation.

An approximate relativistic Hamiltonian should include the following desirable features:

(1) It should be accurate enough to give a close result to the one-electron Dirac or many-electron Dirac–Coulomb(–Breit) Hamiltonian.
(2) It should be efficient and effective to apply to large molecular systems containing heavy elements.
(3) It should be well balanced so as to describe molecular systems containing a wide variety of atoms in the periodic table with the same quality.
(4) It should be variationally stable in order to avoid variational collapse in the sense that at least the non-relativistic limit is obtained correctly.
(5) It should be variational and not perturbative in order to evaluate various energy values and one-electron properties.

The Breit–Pauli (BP) approximation [140] is obtained truncating the Taylor expansion of the Foldy–Wouthuysen (FW) transformed Dirac Hamiltonian [141] up to the $(p/mc)^2$ term. The BP equation has the well-known mass–velocity, Darwin, and spin–orbit operators. Although the BP equation gives reasonable results in the first-order perturbation calculation, it cannot be used in the variational treatment.

One of the shortcomings of the BP approach is that the expansion in $(p/mc)^2$ is not justified in the case where the electronic momentum is too large, e.g. for a Coulomb-like potential. The zeroth-order regular approximation (ZORA) [142,143] can avoid this disadvantage by expanding in $E/(2mc^2 - V)$ up to the first order. The ZORA Hamiltonian is variationally stable. However, the Hamiltonian obtained by a higher order expansion has to be treated perturbatively, similarly to the BP Hamiltonian. Other quasi-relativistic methods have been proposed by Kutzelnigg [144,145] and Dyall [146].

We have developed two quasi-relativistic approaches. One is the RESC method [147–149], and the other is the higher order Douglas–Kroll (DK) method [150–152]. In the following sections we will introduce RESC and higher order DK methods briefly.

20.4.3.2 RESC method

The Dirac equation is equivalent to the Schrödinger–Pauli type equation composed of only the large component

$$\left[V + (\boldsymbol{\sigma}\cdot\mathbf{p})\frac{c^2}{2mc^2 - (V - E)}(\boldsymbol{\sigma}\cdot\mathbf{p}) \right]\Psi^{\mathrm{L}} = e\Psi^{\mathrm{L}} \tag{93a}$$

with the normalization condition

$$\langle \Psi^{L} | 1 + X^{+}X | \Psi^{L} \rangle = 1 \tag{93b}$$

Here the X operator is defined by

$$X \equiv [2mc^2 - (V - E)]^{-1} c(\boldsymbol{\sigma}\cdot\mathbf{p}) \tag{94}$$

If Eq. (93a) could be solved with Eq. (93b), the solution to the Dirac equation can be obtained exactly. However, Eq. (93a) has the total and potential energies in the denominator, and an appropriate approximation is needed. In our strategy, $E - V$ in the denominator is replaced by the classical relativistic kinetic energy (relativistic substitutive correction)

$$T = (m^2c^4 + p^2c^2)^{1/2} - mc^2 \tag{95}$$

This simple approach is referred to as the relativistic scheme by eliminating small components (RESC). The derivation and the form of the RESC Hamiltonian are given in Ref. [147]. The RESC approach has several advantages. It is variationally stable. It can easily be incorporated in non-relativistic *ab initio* programs, and relativistic effects are considered on the same footing with electron correlation. RESC works well for a number of systems, and recent studies have shown it to give results similar to the Douglas–Kroll–Hess (DKH) method for chemical properties, although very large exponents in the basis set can lead to variational collapse in the current RESC approximation, which includes only the lowest truncation of the kinematic operator.

20.4.3.3 Douglas–Kroll method

The Douglas–Kroll (DK) approach [153] can decouple the large and small components of the Dirac spinors in the presence of an external potential by repeating several unitary transformations. The DK transformation is a variant of the FW transformation [141] and adopts the external potential V_{ext} as an expansion parameter instead of the speed of light, c, in the FW transformation. The DK transformation correct to second order in the external potential (DK2) has been extensively studied by Hess and co-workers [154], and has become one of the most familiar quasi-relativistic approaches. Recently, we have proposed the higher order DK method and applied the third-order DK (DK3) method to several systems containing heavy elements.

The first step in the DK transformation consists of a free-particle FW transformation to the Dirac Hamiltonian with the external potential V_{ext}

$$H_D = \begin{pmatrix} V_{ext} + c^2 & c\boldsymbol{\sigma}\cdot\mathbf{p} \\ c\boldsymbol{\sigma}\cdot\mathbf{p} & V_{ext} - c^2 \end{pmatrix} \tag{96}$$

in momentum space. The resulting Hamiltonian yields the free-particle FW Hamiltonian and is also referred to as the first-order DK Hamiltonian. In successive DK transformations, in order to remove odd terms of arbitrary order in the external potential, the unitary operator defined by Douglas and Kroll [153],

$$U_n = (1 + W_n^2)^{1/2} + W_n \tag{97}$$

or the exponential-type unitary operator [150]

$$U_n = \exp(W_n) \tag{98}$$

is employed sequentially. Here W_n is an anti-Hermitian operator of nth order in V_{ext}. The resultant DK Hamiltonian is still a four-component formalism. Its two-component reduction is achieved by replacing β by the unit matrix and $\boldsymbol{\alpha}$ by the 2×2 Pauli spin matrix $\boldsymbol{\sigma}$. In order to correspond to the non-relativistic limit, the resulting two-component Hamiltonian is shifted by $-2c^2$.

The first-order, second-order, and third-order DK (DK1, DK2, and DK3) Hamiltonians in the two-component form are given as

$$H_{\text{DK1}} = E_p - c^2 + E_1 \tag{99}$$

$$H_{\text{DK2}} = H_{\text{DK1}} - \tfrac{1}{2}[W_1, [W_1, E_p]_+]_+ \tag{100}$$

$$H_{\text{DK3}} = H_{\text{DK2}} + \tfrac{1}{2}[W_1, [W_1, E_1]] \tag{101}$$

with

$$E_p = c[(\boldsymbol{\sigma}\cdot\mathbf{p})^2 + c^2]^{1/2} \tag{102}$$

$$E_1 = A(V_{\text{ext}} + RV_{\text{ext}}R)A \tag{103}$$

$$W_1 = A(Rv - vR)A \tag{104}$$

where the kinematical A and R operators and the v operator are defined by

$$A = \left(\frac{E_p + c^2}{2E_p}\right)^{1/2} \tag{105}$$

$$R = \frac{c\boldsymbol{\sigma}\cdot\mathbf{p}}{E_p + c^2} \tag{106}$$

$$v(p,p') = \frac{V_{\text{ext}}(p,p')}{E_p + E_{p'}} \tag{107}$$

and $[a,b]_+$ and $[a,b]$ denote the anti-commutator and the commutator, respectively.

20.4.3.4 Extended Douglas–Kroll transformations applied to the relativistic many-electron Hamiltonian

The DK approach satisfies all of the criteria in Section 20.4.3.1: the DK transformation avoids the high singularity in the FW transformation by adoption of the external potential as an expansion parameter, and thus the DK Hamiltonian is variationally stable. The DK Hamiltonian can be applied to the variational calculation in contrast to the Breit–Pauli Hamiltonian. Criterion (1) is also satisfied by the higher order DK method for the one-electron system. The DK3 Hamiltonian was shown to give excellent agreement with the one-electron Dirac Hamiltonian [150].

By an application of the DK transformation to the relativistic many-electron Hamiltonian, recently, we have shown that the many-electron DK Hamiltonian also gives satisfactory results for a wide variety of atoms and molecules compared with

the DC(B) Hamiltonian [152]. To consider the higher order DK transformation to the two-electron interaction, the present approach adopts the effective one-electron potential in the DHF/DKS operator as an expansion parameter in the DK transformation.

The DHF/DKS operator, Eq. (78), can be written in the same form to the one-electron Dirac Hamiltonian, Eq. (96), by the following replacements:

$$V_{\mathrm{nuc}} + J^{\mathrm{LL}} + J^{\mathrm{SS}} - t_{\mathrm{ex}} K^{\mathrm{XX}} - t_{\mathrm{xc}} V_{\mathrm{xc}} \rightarrow V_{\mathrm{ext}} \tag{108}$$

$$\boldsymbol{\sigma}\cdot\mathbf{p} - \frac{t_{\mathrm{ex}}}{c} K^{\mathrm{XY}} \rightarrow \boldsymbol{\sigma}\cdot\mathbf{p} \tag{109}$$

By substituting these relations into Eqs. (99)–(107), we can straightforwardly obtain the DKn-Fock operators with the DK transformation to the DHF/DKS potential in the two-component DKn-HF/KS equation

$$F_{\mathrm{DK}n}\psi_i = \varepsilon_i \psi_i \tag{110}$$

where ψ_i is the (orthonormalized) two-component DKn spinor and ε_i is its spinor energy. The first-order DK (DK1) operator is given as

$$F_{\mathrm{DK1}} = E_0 - c^2 + E_1 \tag{111}$$

with

$$E_0 = c\left[\left(\boldsymbol{\sigma}\cdot\mathbf{p} - \frac{t_{\mathrm{ex}}}{c} K^{\mathrm{LS}}\right)\left(\boldsymbol{\sigma}\cdot\mathbf{p} - \frac{t_{\mathrm{ex}}}{c} K^{\mathrm{SL}}\right) + c^2\right]^{1/2} \tag{112}$$

$$\begin{aligned} E_1 = {} & A(V_{\mathrm{nuc}} + J^{\mathrm{LL}} + J^{\mathrm{SS}} - t_{\mathrm{ex}} K^{\mathrm{LL}} - t_{\mathrm{xc}} V_{\mathrm{xc}})A \\ & + AR^{\mathrm{LS}}(V_{\mathrm{nuc}} + J^{\mathrm{LL}} + J^{\mathrm{SS}} - t_{\mathrm{ex}} K^{\mathrm{SS}} - t_{\mathrm{xc}} V_{\mathrm{xc}})R^{\mathrm{SL}}A \end{aligned} \tag{113}$$

where the A and R^{XY} operators are defined by

$$A = \left(\frac{E_0 + c^2}{2E_0}\right)^{1/2} \tag{114}$$

$$R^{\mathrm{XY}} = \frac{c}{E_0 + c^2}\left(\boldsymbol{\sigma}\cdot\mathbf{p} - \frac{t_{\mathrm{ex}}}{c} K^{\mathrm{XY}}\right) \tag{115}$$

In this approach, the density matrix is evaluated self-consistently with both the large and small component spinors, φ_i^{L} and φ_i^{S}, which can be reconstructed from the free-particle FW spinors ψ_i in the Schrödinger picture

$$\varphi_i^{\mathrm{L}} = A\psi_i \tag{116}$$

$$\varphi_i^{\mathrm{S}} = R^{\mathrm{SL}} A \psi_i \tag{117}$$

It is easy to verify that the DK1 operator, Eq. (111), is equivalent to the Fock operator derived from the no-pair or free-particle FW Hamiltonian. Likewise, the higher order DK operators are also derived straightforwardly by repeating the DK transformations, though their formulae are omitted only because of their lengthy forms.

References pp. 554–557

As molecular applications of the extended DK approach, we have calculated the spectroscopic constants for At_2: equilibrium bond lengths (R_e), harmonic frequencies (ω_e), rotational constants (B_e), and dissociation energies (D_e). A strong spin–orbit effect is expected for these properties because the outer p orbital participates in their molecular bonds. Electron correlation effects were treated by the hybrid DFT approach with the B3LYP functional. Since several approximations to both the one-electron and two-electron parts of the DK Hamiltonian are available, we define that the DK$n1$ + DK$n2$ Hamiltonian ($n1$, $n2 = 1-3$) denotes the DK Hamiltonian with DK$n1$ and DK$n2$ transformations for the one-electron and two-electron parts, respectively. The DK$n1$ + DK1 Hamiltonian is equivalent to the no-pair DK$n1$ Hamiltonian. For the two-electron part the electron–electron Coulomb operator in the non-relativistic form can also be adopted. The DK$n1$ Hamiltonian with the non-relativistic Coulomb operator is denoted by the DK$n1$ + NR Hamiltonian.

Table 20.13 shows the results for At_2 obtained by approximate DK schemes in comparison with four-component DKS results. The DK results for the spectroscopic constants and the total energy in the equilibrium geometry (E_{tot}) become closer to the DKS results as the level of theory is improved. The highest level of theory, DK3–DK3, as well as DK3–DK2, gives fairly good agreement with the four-component result for At_2. The DK3–DK3 operator yields $R_e = 3.1102$ Å, $\omega_e = 102.3$ cm^{-1}, and $D_e = 0.546$ eV, the corresponding four-component DKS values being $R_e = 3.1121$ Å, $\omega_e = 102.0$ cm^{-1}, and $D_e = 0.542$ eV. The discrepancy between DK3–DK3 and DKS Hamiltonians is $\Delta R_e = 0.0019$ Å, $\Delta\omega_e = 0.3$ cm^{-1}, and $\Delta D_e = 0.004$ eV.

By comparison between the DK3–DK3 and DK3–NR results, it can be seen that two-electron relativistic effects are comparatively large, especially in the dimer; the bond length decreases by 0.06 Å, the frequency increases by 7 cm^{-1}, the rotational constant increases by 0.0006 cm^{-1}, and the dissociation energy increases by 0.12 eV. Neglect of the relativistic correction to the electron–electron interaction yields inferior results and gives relatively large deviations from the DK3–DK3 or DKS result. It is interesting that the importance of the two-electron DK correction for the bond length is shown, because it has been believed so far that the bond length is scarcely affected by the relativistic

Table 20.13 Bond lengths (R_e), harmonic frequencies (ω_e), rotational constants (B_e), dissociation energies (D_e), and total energies (E_{tot}) in the equilibrium geometry of At_2 with B3LYP

Hamiltonian	R_e (Å)	ω_e (cm^{-1})	B_e (cm^{-1})	D_e (eV)	E_{tot} (a.u.)
DKS	3.1121	102.0	0.0166	0.542	−45838.2314
DK3–DK3	3.1102	102.3	0.0166	0.546	−45841.9720
DK3–DK3	3.1080	102.3	0.0166	0.552	−45849.7971
(no mod. V_{xc})[a]					
DK3–DK2	3.1108	102.3	0.0166	0.545	−45842.2586
DK3–DK1	3.1074	102.6	0.0166	0.552	−45839.6417
DK3–NR	3.1697	95.5	0.0160	0.429	−45849.7240
DK2–DK2	3.1013	103.0	0.0167	0.561	−45773.7217

[a]Results without the relativistic modification to V_{xc}.

correction to the electron–electron interaction, while the harmonic frequency and the dissociation energy are often influenced.

The first-order DK correction to the electron–electron interaction is satisfactory also in molecular systems, as well as the atomic case. The deviation of DK3–DK1 from DK3–DK3 is $\Delta R_e = 0.0028$ Å, $\Delta\omega_e = 0.3\ cm^{-1}$, and $\Delta D_e = 0.006$ eV for At_2.

In the DFT approach with our general DK transformation, the exchange-correlation potential, V_{xc}, is corrected relativistically. The effect on the DK transformation to the exchange-correlation potential was estimated by comparison with the result without the relativistic modification to V_{xc} ((no mod. V_{xc}) in Table 20.13). Compared with the full DK3–DK3 approach, neglect of the relativistic DK correction to the exchange-correlation potential hardly affects the calculated spectroscopic values; its effect merely contributes 0.002 Å for R_e and 0.006 eV for D_e and does not affect ω_e and B_e for the At dimer. Thus, it is found that the relativistic correction to the electron–electron interaction contributes mainly to the Coulomb potential, not to the exchange-correlation potential.

In consequence, the several numerical results including the present results show that the third-order DK transformation to both one-electron and two-electron Hamiltonians gives excellent agreement with the four-component relativistic approach. The first-order DK correction to the two-electron interaction is shown to be satisfactory for both atomic and molecular systems.

20.5 SUMMARY

The recent advances in electronic structure theory achieved in our research group have been reviewed. New theory/algorithm has been implemented and incorporated into the program package, UTCHEM [155]. Software forms a basis for computational chemistry. It is not an easy task for an individual/group to develop a comprehensive new program package in quantum chemistry from scratch. Several years ago, we decided to accept this challenge. In view of the availability of such good programs as GAUSSIAN, GAMESS, MOLCAS, NWCHEM, etc., one may question the relevance of a new program package. We have three arguments for our project. (1) First, we believe that healthy competition is very important in science. (2) Second, we can have a good harvest by doing research using other programs, but it is an abortive flower. We could not make a true breakthrough if we were circumscribed by current software limitations. (3) Third, in spite of the excellent performance of other programs, there are important and powerful methods that others cannot yet handle. We have developed new methodologies in quantum chemistry, particularly the multireference-based perturbation theory for describing chemical reactions and excited states, relativistic molecular theory to treat heavy elements, parameter-free (less) and long-range corrected (LC) exchange and correlation functionals in DFT, highly efficient algorithms for calculating molecular integrals over generally contracted Gaussians, etc. UTCHEM is a research product of our work to develop new and better theoretical methods in quantum chemistry. Most of the codes have been developed recently by Hirao's group at the University of Tokyo. The basic philosophy behind UTCHEM is to develop methods that allow an accurate and efficient computational chemistry of electronic structure problems for molecular systems in both the ground and

excited states. UTCHEM also contains codes for well-developed methods such as MPn, CI, CC, etc., which are standard in most quantum chemistry programs. We are aiming ultimately at better performance than other programs. UTCHEM has been released. If you want more information on UTCHEM, visit http://utchem.qcl.t.u-tokyo.ac.jp/.

20.6 REFERENCES

1 K. Hirao, Chem. Phys. Lett., 190 (1992) 374.
2 K. Hirao, Chem. Phys. Lett., 196 (1992) 397.
3 K. Hirao, Chem. Phys. Lett., 201 (1993) 59.
4 K. Hirao, Int. J. Quantum Chem. S, 26 (1992) 517.
5 H. Nakano, J. Chem. Phys., 99 (1993) 9873.
6 H. Nakano, Chem. Phys. Lett., 207 (1993) 372.
7 H. Nakano, M. Yamanishi and K. Hirao, Trends Chem. Phys., 6 (1997) 167.
8 K. Hirao, K. Nakayama, T. Nakajima and H. Nakano, in: J. Leszczynski (Ed.), Computational chemistry, Vol. 4, World Scientific, Singapore, 1999, pp. 227–270.
9 H. Nakano, T. Nakajima, T. Tsuneda and K. Hirao, J. Mol. Struct. (THEOCHEM), 573 (2001) 91.
10 T. Nakajima, T. Tsuneda, H. Nakano and K. Hirao, J. Theor. Comput. Chem., 1 (2002) 109.
11 C. Møller and M.S. Plesset, Phys. Rev., 46 (1934) 618.
12 B.H. Brandow, Rev. Mod. Phys., 39 (1967) 771.
13 I. Lindgren, Int. J. Quantum Chem. Symp., 12 (1978) 33.
14 B.H. Brandow, Int. J. Quantum Chem., 15 (1979) 207.
15 G. Hose and U. Kaldor, J. Phys. B, 12 (1981) 3827.
16 K.F. Freed and M.G. Sheppard, J. Chem. Phys., 75 (1981) 4507, see also p. 4525.
17 H. Primas, Helv. Phys. Acta, 34 (1961) 331.
18 H. Primas, Rev. Mod. Phys., 35 (1963) 710.
19 B. Kirtman, J. Chem. Phys., 49 (1968) 3890, 75 (1981) 798.
20 P.R. Certain and J.O. Hirschfelder, J. Chem. Phys., 52 (1970) 5977, 53 (1970) 2992.
21 J.O. Hirschfelder, Chem. Phys. Lett., 54 (1978) 1.
22 T.H. Schucan and H.A. Weidenmuller, Ann. Phys. N.Y., 76 (1973) 483.
23 K. Wolinski, H.L. Sellers and P. Pulay, Chem. Phys. Lett., 140 (1987) 225.
24 J.J.W. McDouall, K. Peasley and M.A. Robb, Chem. Phys. Lett., 148 (1988) 183.
25 K. Andersson, P. Malmqvist, B.O. Roos, A.J. Sadlej and K. Wolinski, J. Phys. Chem., 94 (1990) 5483.
26 K. Andersson, P. Malmqvist and B.O. Roos, J. Chem. Phys., 96 (1992) 1218.
27 R.B. Murphy and R.P. Messmer, Chem. Phys. Lett., 183 (1991) 443.
28 R.B. Murphy and R.P. Messmer, J. Chem. Phys., 97 (1992) 4170.
29 P.M. Kozlowski and E.R. Davidson, J. Chem. Phys., 100 (1994) 3672.
30 K.G. Dyall, J. Chem. Phys., 102 (1995) 4909.
31 Y. Kobayashi, H. Nakano and K. Hirao, Chem. Phys. Lett., 336 (2001) 529.
32 C.W. Bauschlicher and P.R. Taylor, J. Chem. Phys., 85 (1986) 6510.
33 P. Jensen and P.R. Bunker, J. Chem. Phys., 89 (1988) 1327.
34 S. Koda, Chem. Phys., 66 (1982) 383.
35 H. Nakano, J. Nakatani and K. Hirao, J. Chem. Phys., 114 (2001) 1133.
36 H. Nakano, R. Uchiyama and K. Hirao, J. Comput. Chem., 23 (2002) 1166.
37 H. Nakano, K. Nakayama, K. Hirao and M. Dupuis, J. Chem. Phys., 106 (1997) 4912.
38 W.F. Polik, D.R. Guyer and C.B. Moore, J. Chem. Phys., 92 (1990) 3453.
39 M.R.J. Hachey, P.J. Bruna and F. Grein, J. Phys. Chem., 99 (1995) 8050.
40 M. Merchán and B.O. Roos, Theor. Chim. Acta, 92 (1995) 227.
41 S.R. Gwaltney and R.J. Bartlett, Chem. Phys. Lett., 241 (1995) 26.
42 C.M. Hadad, J.B. Foresman and K.B. Wiberg, J. Phys. Chem., 97 (1993) 4293.
43 M. Head-Gordon, R.J. Rico, M. Oumi and T.J. Lee, Chem. Phys. Lett., 219 (1994) 21.
44 H. Nakatsuji, K. Ohta and K. Hirao, J. Chem. Phys., 75 (1981) 2952.

45 Y. Kurashige, H. Nakano and K. Hirao, J. Phys. Chem. A, 108 (2004) 3064.
46 J.M. Rintelman and M.S. Gordon, J. Chem. Phys., 115 (2001) 1795.
47 K.W. Sattelmeyer, H.F. Schaefer, III and J.F. Stanton, J. Chem. Phys., 116 (2002) 9151.
48 K.A. Peterson, D.E. Woon and T.H. Dunning, Jr., J. Chem. Phys., 100 (1994) 7410.
49 J.F. Stanton, J. Gauss and O. Christiansen, J. Chem. Phys., 114 (2001) 2993.
50 K. Hirao, H. Nakano, K. Nakayama and M. Dupuis, J. Chem. Phys., 105 (1996) 9227.
51 K. Hirao, H. Nakano and K. Nakayama, J. Chem. Phys., 107 (1997) 9966.
52 B. Lam, M.W. Schmidt and K. Ruedenberg, J. Phys. Chem., 89 (1985) 2221.
53 T.R. Cundari and M.S. Gordon, J. Am. Chem. Soc., 113 (1991), 114 (1992) 539.
54 D.L. Cooper, J. Gerratt and M. Raimond, Nature, 323 (1986) 699.
55 D.L. Cooper, J. Gerratt and M. Raimond, Adv. Chem. Phys., 27 (1987) 319.
56 W.J. Hunt, P.J. Hay and W.A. Goddard, J. Chem. Phys., 57 (1972) 738.
57 W.A. Goddard and L.B. Harding, Annu. Rev. Phys. Chem., 29 (1978) 363.
58 P.C. Hiberty, J.P. Flament and E. Noizet, Chem. Phys. Lett., 189 (1992) 259.
59 P. Maitre, J.M. Lefour, G. Ohanessian and P.C. Hiberty, J. Phys. Chem., 94 (1990) 4082.
60 H. Nakano, K. Sorakubo, K. Nakayama and K. Hirao, in: D.L. Cooper (Ed.), Valence bond theory, Theoretical and computational chemistry, Vol. 10, Elsevier, Amsterdam, 2001, pp. 55–77.
61 W. Kohn and L.J. Sham, Phys. Rev. A, 140 (1995) 1133.
62 R.G. Parr and W. Yang, Density-functional theory of atoms and molecules, Oxford University Press, New York, 1989.
63 R.M. Dreizler and E.K.U. Gross, Density-functional theory: An approach to the quantum many-body problem, Springer, Berlin, 1990.
64 A.D. Becke, Phys. Rev. A, 38 (1988) 3098.
65 J.P. Perdew and Y. Wang, in: P. Ziesche, H. Eschrig (Eds.), Electronic structure of solids '91, Akademie, Berlin, 1991.
66 J.P. Perdew, K. Burke and M. Ernzerhof, Phy. Rev. Lett., 77 (1996) 3865.
67 T. Tsuneda and K. Hirao, Phys. Rev. B, 62 (2000) 15527.
68 J.C. Slater, Phys. Rev., 81 (1951) 385.
69 T. Tsuneda, T. Suzumura and K. Hirao, J. Chem. Phys., 111 (1999) 5656.
70 T. Tsuneda, M. Kamiya, N. Morinaga and K. Hirao, J. Chem. Phys., 114 (2001) 6505.
71 L. Kleinman and S. Lee, Phys. Rev. B, 37 (1988) 4634.
72 A.D. Becke, J. Chem. Phys., 98 (1993) 5648.
73 C. Lee, W. Yang and R.G. Parr, Phys. Rev. B, 37 (1988) 785.
74 S.H. Vosko, L. Wilk and M. Nusair, Can. J. Phys., 58 (1980) 1200.
75 A.D. Becke, J. Chem. Phys., 107 (1997) 8554.
76 J.P. Perdew, K. Burke and M. Ernzerhof, J. Chem. Phys., 105 (1996) 9982.
77 M. Levy, J.P. Perdew and V. Sahni, Phys. Rev. A, 30 (1984) 2745.
78 R. van Leeuwen and E.J. Baerends, Phys. Rev. A, 49 (1994) 2421.
79 D.J. Tozer and N.C. Handy, J. Chem. Phys., 109 (1988) 10180.
80 D.J. Tozer, J. Chem. Phys., 112 (1999) 3507.
81 J.P. Perdew and A. Zunger, Phys. Rev. B, 23 (1981) 5048.
82 B.G. Johnson, C.A. Gonzales, P.M.W. Gill and J.A. Pople, Chem. Phys. Lett., 221 (1994) 100.
83 X. Tong and S. Chu, Phys. Rev. A, 55 (1997) 3406.
84 T. Tsuneda, M. Kamiya and K. Hirao, J. Comput. Chem., 24 (2003) 1592.
85 A. Savin, in: J.M. Seminario (Ed.), Recent developments and applications of modern density functional theory, Elsevier, Amsterdam, 1996, p. 327.
86 H. Iikura, T. Tsuneda, T. Yanai and K. Hirao, J. Chem. Phys., 115 (2001) 3540.
87 J. Heyd, G.E. Scuseria and M. Ernzerhof, J. Chem. Phys., 118 (2003) 8207.
88 J. Heyd and G.E. Scuseria, J. Chem. Phys., 120 (2004) 7274.
89 T. Leininger, H. Stoll, H.-J. Werner and A. Savin, Chem. Phys. Lett., 275 (1997) 151.
90 H.L. Williams and C.F. Chabalowski, J. Phys. Chem., 105 (2001) 646.
91 Y. Andersson, D.C. Langreth and B.I. Lundqvist, Phys. Rev. Lett., 76 (1996) 102.
92 K. Rapcewicz and N.W. Ashcroft, Phys. Rev. B, 44 (1991) 4032.

93 W. Kohn, Y. Meier and D.E. Makarov, Phys. Rev. Lett., 80 (1998) 4153.
94 M. Kamiya, T. Tsuneda and K. Hirao, J. Chem. Phys., 117 (2002) 6010.
95 T. Tsuneda, T. Suzumura and K. Hirao, J. Chem. Phys., 110 (1999) 10664.
96 R. Krishnan, J.S. Binkley, R. Seeger and J.A. Pople, J. Chem. Phys., 72 (1980) 650.
97 A.D. McLean and G.S. Chandler, J. Chem. Phys., 72 (1980) 5639.
98 M.J. Frisch, J.A. Pople and J.S. Binkley, J. Chem. Phys., 80 (1984) 3265.
99 S.F. Boys and F. Bernardi, Mol. Phys., 19 (1970) 553.
100 C. Adamo and V. Barone, J. Chem. Phys., 118 (1998) 664.
101 Q. Wu and W. Yang, J. Chem. Phys., 116 (2002) 515.
102 Y. Tawada, T. Tsuneda, S. Yanagisawa, T. Yanai and K. Hirao, J. Chem. Phys., 120 (2004) 8425.
103 H. Nakatsuji, Chem. Phys. Lett., 59 (1978) 362.
104 R. Krishnan, J.S. Binkley, R. Seeger and J.A. Pople, J. Chem. Phys., 72 (1980) 650.
105 A.D. McLean and G.S. Chandler, J. Chem. Phys., 72 (1980) 5639.
106 A. Dreuw, J.L. Weisman and M. Head-Gordon, J. Chem. Phys., 119 (2003) 2943.
107 S. Yanagisawa, T. Tsuneda and K. Hirao, J. Chem. Phys., 112 (2000) 545.
108 S. Yanagisawa, T. Tsuneda and K. Hirao, J. Comput. Chem., 22 (2001) 1995.
109 T. Tsuneda, S. Tokura and K. Hirao, in preparation.
110 A.J.H. Wachters, J. Chem. Phys., 52 (1970) 1033.
111 A.J.H. Wachters, IBM Tech. Rep., RJ584 (1969).
112 C.W. Bauschlicher, Jr., S.R. Langhoff and L.A. Barnes, J. Chem. Phys., 91 (1989) 2399.
113 T. Tsuneda, N. Kawakami and K. Hirao, in preparation.
114 M. Kamiya, H. Sekino, T. Tsuneda and K. Hirao, J. Chem. Phys., in press.
115 T.H. Dunning Jr., to be published.
116 A.J. Sadlej, Theor. Chim. Acta, 81 (1992) 339.
117 M.E. Casida, C. Jamorski, K.C. Casida and D.R. Salahub, J. Chem. Phys., 108 (1998) 4439.
118 T. Nakajima, T. Yanai and K. Hirao, J. Comput. Chem., 23 (2002) 847.
119 T. Yanai, T. Nakajima, Y. Ishikawa and K. Hirao, in: K. Hirao, Y. Ishikawa (Eds.), Recent advances in relativistic effects in chemistry, World Scientific, Singapore, 2004, pp. 221.
120 T. Nakajima, Bull. Kor. Chem. Soc., 24 (2003) 809.
121 Y. Ishikawa and K. Koc, Phys. Rev. A, 56 (1997) 1295; M.J. Vilkas, Y. Ishikawa and K. Koc, Phys. Rev. E, 58 (1998) 5096; M.J. Vilkas, Y. Ishikawa and K. Hirao, Chem. Phys. Lett., 321 (2000) 243.
122 E. Eliav, U. Kaldor and Y. Ishikawa, Phys. Rev. A, 53 (1996) 3050.
123 L. Visscher, O. Visser, H. Aerts, H. Merenga and W.C. Nieuwpoort, Comput. Phys. Commun., 81 (1994) 120.
124 T. Saue, K. Fægri, T. Helgaker and O. Gropen, Mol. Phys., 91 (1997) 937.
125 H.M. Quiney, H. Skaane and I.P. Grant, Adv. Quantum Chem., 32 (1999) 1; I.P. Grant and H.M. Quiney, Int. J. Quantum Chem., 80 (2000) 283.
126 A. Mohanty and E. Clementi, Int. J. Quantum. Chem., 39 (1991) 487.
127 L. Pisani and E. Clementi, J. Comput. Chem., 15 (1994) 466.
128 K.G. Dyall, P.R. Taylor, K. Fægrei and H. Partridge, J. Chem. Phys., 95 (1991) 2583.
129 Y. Ishikawa, R.C. Binning and K.M. Sando, Chem. Phys. Lett., 101 (1983) 111; Y. Ishikawa, R.C. Binning and K.M. Sando, Chem. Phys. Lett., 105 (1984) 189; Y. Ishikawa, R.C. Binning and K.M. Sando, Chem. Phys. Lett., 117 (1985) 444; R.E. Stanton and S. Havriliak, J. Chem. Phys., 81 (1984) 1910.
130 T. Yanai, T. Nakajima, Y. Ishikawa and K. Hirao, J. Chem. Phys., 114 (2001) 6525.
131 T. Yanai, H. Iikura, T. Nakajima, Y. Ishikawa and K. Hirao, J. Chem. Phys., 115 (2001) 8267.
132 T. Yanai, T. Nakajima, Y. Ishikawa and K. Hirao, J. Chem. Phys., 116 (2002) 10122.
133 M. Head-Gordon and J.A. Pople, J. Chem. Phys., 89 (1988) 5777.
134 K. Ishida, Int. J. Quantum Chem., 59 (1996) 209; K. Ishida, J. Chem. Phys., 109 (1998) 881; K. Ishida, J. Comput. Chem., 19 (1998) 923; K. Ishida, J. Chem. Phys., 111 (1999) 4913.
135 T. Nakajima and K. Hirao, J. Chem. Phys., 121 (2004) 3438.
136 R.A. Friesner, Chem. Phys. Lett., 116 (1985) 39.
137 R.A. Friesner, J. Chem. Phys., 85 (1986) 1462.

138 K.P. Huber and G. Herzberg, Molecular structure IV, constants of diatomic molecules, Van Nostrand, New York, 1979.
139 B. Simard and P.A. Hackett, J. Mol. Spectrosc., 412 (1990) 310.
140 H.A. Bethe and E.E. Salpeter, Quantum mechanics of one- and two-electron atoms, Springer, Berlin, 1957.
141 L.L. Foldy and S.A. Wouthuysen, Phys. Rev., 78 (1950) 29.
142 E. van Lenthe, E.J. Baerends and J.G. Snijders, J. Chem. Phys., 99 (1993) 4597.
143 Ch. Chang, M. Pelissier and Ph. Durand, Phys. Scr., 34 (1986) 394.
144 W. Kutzelnigg, Z. Phys. D, 11 (1989) 15.
145 W. Kutzelnigg, Z. Phys. D, 15 (1990) 27.
146 K.G. Dyall, J. Chem. Phys., 100 (1994) 2118.
147 T. Nakajima and K. Hirao, Chem. Phys. Lett., 302 (1999) 383.
148 T. Nakajima, T. Suzumura and K. Hirao, Chem. Phys. Lett., 304 (1999) 271.
149 D. Fedorov, T. Nakajima and K. Hirao, Chem. Phys. Lett., 335 (2001) 183.
150 T. Nakajima and K. Hirao, J. Chem. Phys., 113 (2000) 7786.
151 T. Nakajima and K. Hirao, Chem. Phys. Lett., 329 (2000) 511.
152 T. Nakajima and K. Hirao, J. Chem. Phys., 119 (2003) 4105.
153 M. Douglas and N.M. Kroll, Ann. Phys. N.Y., 82 (1974) 89.
154 B.A. Hess, Phys. Rev. A, 33 (1986) 3742; G. Jansen and B.A. Hess, Phys. Rev. A, 39 (1989) 6016.
155 T. Yanai, M. Kamiya, Y. Kawashima, T. Nakajima, H. Nakano, Y. Nakao, H. Sekino, T. Tsuneda, S. Yanagisawa and K. Hirao, UTCHEM.